Gassmöller, R., Dannberg, J., Bredow, E., Steinberger, B., Torsvik, T. H. (2016): Major influence of plume-ridge interaction, lithosphere thickness variations and global mantle flow on hotspot volcanism - the example of Tristan. - *Geochemistry Geophysics Geosystems (G3)*, *17*, 4, pp. 1454—1479.

DOI: http://doi.org/10.1002/2015GC006177

AGU PUBLICATIONS

Geochemistry, Geophysics, Geosystems

RESEARCH ARTICLE
10.1002/2015GC006177

Key Points:
- The Tristan and Gough chains can be explained by a single plume interacting with the nearby ridge
- The crustal thickness profile across the Walvis Ridge can be explained by a plume feeding into the southern rift part
- Neglecting global flow mispredicts plume excess temperature by 50 K and melt volume by 40%

Supporting Information:
- Supporting Information S1
- Movie S1
- Movie S2
- Data Set S1
- Data Set S2
- Data Set S3
- Data Set S4
- Data Set S5

Correspondence to:
R. Gassmöller,
gassmoeller@math.tamu.edu

Citation:
Gassmöller, R., J. Dannberg, E. Bredow, B. Steinberger, and T. H. Torsvik (2016), Major influence of plume-ridge interaction, lithosphere thickness variations, and global mantle flow on hotspot volcanism—The example of Tristan, *Geochem. Geophys. Geosyst.*, *17*, 1454–1479, doi:10.1002/2015GC006177.

Received 12 NOV 2015
Accepted 16 MAR 2016
Accepted article online 21 MAR 2016
Published online 29 APR 2016

Major influence of plume-ridge interaction, lithosphere thickness variations, and global mantle flow on hotspot volcanism—The example of Tristan

Rene Gassmöller[1,2], Juliane Dannberg[1,2], Eva Bredow[1], Bernhard Steinberger[1,3], and Trond H. Torsvik[3,4,5]

[1]GFZ German Research Centre for Geosciences, Section 2.5, Telegrafenberg, Potsdam, Germany, [2]Now at Department of Mathematics, Texas A&M University, College Station, Texas, USA, [3]Centre for Earth Evolution and Dynamics, University of Oslo, Oslo, Norway, [4]Geological Survey of Norway (NGU), Trondheim, Norway, [5]School of Geosciences, University of Witwatersrand, Wits, South Africa

Abstract Hotspot tracks are thought to originate when mantle plumes impinge moving plates. However, many observed cases close to mid-ocean ridges do not form a single age-progressive line, but vary in width, are separated into several volcanic chains, or are distributed over different plates. Here we study plume-ridge interaction at the example of the Tristan plume, which features all of these complexities. Additionally, the South Atlantic formed close to where plume volcanism began, opening from the south and progressing northward with a notable decrease in magmatism across the Florianopolis Fracture Zone. We study the full evolution of the Tristan plume in a series of three-dimensional regional models created with the convection code ASPECT. We then compute crustal thickness maps and compare them to seismic profiles and the topography of the South Atlantic. We find that the separation of volcanism into the Tristan and Gough chain can be explained by the position of the plume relative to the ridge and the influence of the global flow field. Plume material below the off-ridge track can flow toward the ridge and regions of thinner lithosphere, where decompression melting leads to the development of a second volcanic chain resembling the Tristan and Gough hotspot tracks. Agreement with the observations is best for a small plume buoyancy flux of 500 kg/s or a low excess temperature of 150 K. The model explains the distribution of syn-rift magmatism by hot plume material that flows into the rift and increases melt generation.

1. Motivation

Around 175 million years ago, the southern supercontinent Gondwana, which had existed since Late Precambrian times but amalgamated forming Pangea in the Carboniferous [*Torsvik and Cocks*, 2013], first split into West (including Africa and South America) and East Gondwana. In Late Jurassic-Early Cretaceous times, the parts that eventually became Africa and South America started rifting apart, followed by the opening of the South Atlantic around 130 million years ago. How, in broad terms, this process occurred kinematically, is relatively well known. Already *Wegener* [1915] reconstructed continents relative to each other in a way rather similar to modern-day reconstructions such as *Torsvik et al*. [2009, 2010], which are much better constrained through time mainly based on seafloor magnetic anomalies and fracture zones [*Müller et al*., 2008]. The early opening history of the South Atlantic, however, is convoluted by the fact that there are no magnetic anomalies between approximately 121 and 84 million years ago (the Cretaceous Normal Superchron, see Figure 1).

Yet the role of mantle plumes during continental breakup remains controversial. In the South Atlantic, in particular the Tristan plume may have played an important role. Many of the features usually associated with mantle plumes are observed in this region. (1) Active intraplate volcanism occurs on Tristan da Cunha and Gough Island. (2) The Walvis Ridge is a chain of seamounts thought to be generated as volcanic "hotspot track" as the African plate moves over the plume upwelling [*Morgan*, 1971]. (3) Volcanism along the track is age progressive, with ages getting older further away from the hotspot—see *O'Connor and Duncan* [1990], *O'Connor and le Roex* [1992], *Rohde et al*. [2013], and references cited therein. Geometry and age progression of the track fits with a global model of plate motions over hotspots that are either fixed [*Morgan*, 1971] or

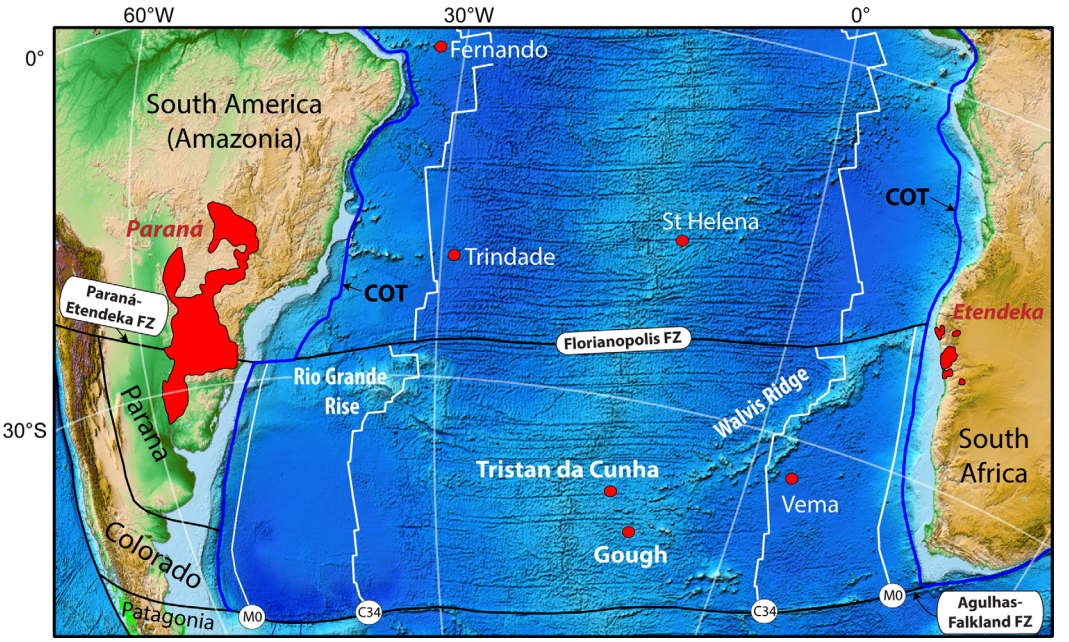

Figure 1. Simplified map of the South Atlantic Ocean draped on ETOPO1. The Florianopolis and Agulhas-Falkland Fracture Zones (FZ) are highlighted along with isochrons M0 (approximately 121 Ma) and C34 (approximately 84 Ma), and we also show some active hotspots and the Paraná-Etendeka large igneous province in Brazil and Namibia. South America is divided into four blocks and the Paraná-Etendeka Fault Zone (active until 126.9 Ma in the model of *Torsvik et al.* [2009]) separates Amazonia from Paraná and Colorado. Colorado and Patagonia were juxtaposed at about 132 Ma but the bulk of dextral strike-slip faulting ceased at around 160 Ma. COT, Continent Ocean Transition Zone.

slowly moving [*Doubrovine et al.*, 2012]. (4) Apart from the narrow volcanic tracks, there is also a wider topographic swell [*Davies*, 1988; *Sleep*, 1990]. (5) There is a geochemical anomaly along the nearby ridge [*Schilling*, 1991]. (6) The Paraná-Etendeka flood basalts, a large igneous province (LIP), is thought to represent the eruption of the initial plume head [*Richards et al.*, 1989]. Moreover, both the reconstructed location where the Paraná-Etendeka flood basalts initially erupted, and the current hotspot location directly overlie the margin of the African Large Low Shear Velocity Province (LLSVP), a likely zone for the generation of plumes in the deepest mantle [*Torsvik et al.*, 2006].

However, the interpretation of observations in terms of the mantle plume model is complicated in particular due to the proximity of plume and ridge through much of their history. As proposed long ago by *Morgan* [1978], plumes can interact with ridges in their vicinity: Volcanism may often not (only) occur directly above the plume, rather plume material may flow at the base of the lithosphere toward regions of thinner lithosphere—a process coined "upside-down drainage" [*Sleep*, 1997]. Moreover, plume material may be sucked toward plate boundaries with negative dynamic pressures, resulting from divergent plate motion (such as the mid-oceanic ridge, but also the transtensional Paraná-Etendeka fault zone). Both mechanisms can lead to additional decompression melting and eruptions at the ridge and could be responsible for the fact that there are roughly parallel volcanic tracks. The one ending at Tristan da Cunha would then correspond to volcanism at or near the ridge, and the one ending at Gough Island would be due to eruptions directly above the plume. Since the onset of continental rifting predates the onset of flood basalt volcanism [*de Assis Janasi et al.*, 2011], the mantle plume cannot have been the cause of rifting. Yet the generation of ocean floor in the South Atlantic only began after the plume head eruption. Therefore, it is possible that the extension of continents concentrates above mantle plumes, which thus may assist in continental breakup [*Buiter*, 2014; *Burov and Gerya*, 2014].

Recent results have provided more details on volcanics and crustal structure, and their relation to the opening of the South Atlantic and the Tristan plume (also called Tristan-Gough plume): *Heit et al.* [2015] show that seismic anomalies on the Namibian margin, when interpreted as magmatic underplating, indicate that plume influence was more limited than would be expected if a large plume head impinged the African plate. Similarly, results of deep crustal seismic sounding [*Ryberg et al.*, 2015] suggest a locally confined influence of

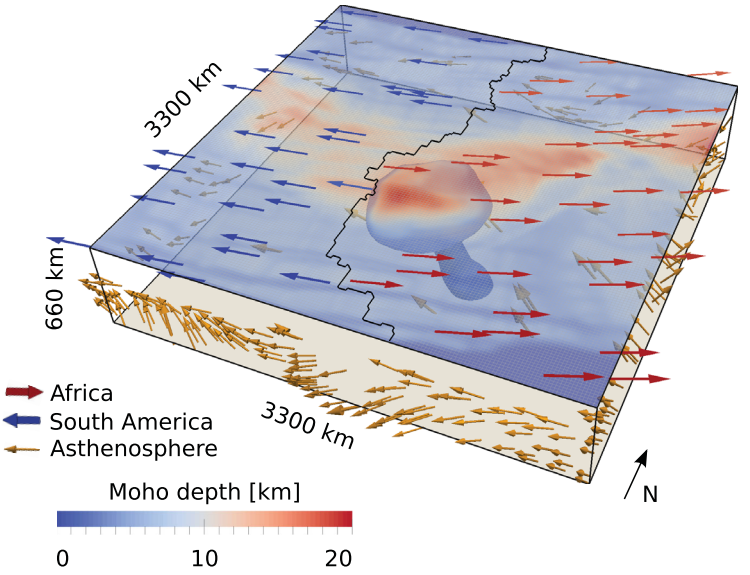

Figure 2. Geometry and velocity boundary conditions of the presented convection model. Red and blue arrows denote the prescribed plate motions at the top. Side boundary velocities within the lithosphere are identical to the plate motions, and asthenosphere boundary velocities at the sides and the bottom (yellow arrows) are taken from a global mantle convection model. The transition between plate and asthenospheric velocities is smoothed by a hyperbolic tangent interpolation function. An additional plume inflow is enforced at the bottom boundary.

the plume head affected by preexisting lithosphere structure. *Fromm et al*. [2015] show large crustal thickness variations across the Florianopolis Fracture Zone along the Namibia continental margin. *O'Connor and Jokat* [2015a] discuss how separated segments of age-progressive intraplate volcanics may be related to a single plume. *O'Connor and Jokat* [2015b] propose that new age dates from ocean drill sites across the Central Walvis Ridge can be explained by interaction of that plume and the South Atlantic Ridge. While theoretical studies indicate that a single plume could be responsible for some of these structures [*Sleep*, 2002], it is still not clear if and how plume-ridge interaction can explain these observations dynamically.

In order to improve our understanding of these results and the role of the Tristan plume in the context of plume-ridge interaction, we have devised a numerical convection model. This model is not fully dynamic in that a given plate reconstruction is applied as surface boundary condition. We follow an approach previously taken by *Mihalffy et al*. [2008] for the Iceland plume, setting up a high-resolution box model with boundary conditions obtained from a coarser global model. In particular, the large-scale flow field and the plume position are obtained from a global flow model, which infers its present-day temperature from seismic tomography and is then advected backward in time. We study the flow of the hot plume material in interaction with the mid-ocean ridge in the regional model and where high temperatures lead to melting and excess crustal production. Finally, we compare our model results with observed locations of volcanism, and by varying important model parameters, such as plume buoyancy flux, lithosphere thickness, and the initial plume location, we aim at obtaining an improved agreement. In this way, we can assess whether the plume model is suitable at all to explain the observed distribution of volcanism and crustal thickness, and if so, for which parameters.

2. Model Setup

2.1. Boundary and Initial Conditions

The model domain is a three-dimensional Cartesian box as shown in Figure 2. It comprises the upper mantle and transition zone in vertical direction and extends 3300 km × 3300 km horizontally. The initial conditions correspond to the setting of the South Atlantic 140 million years ago, before the breakup of South America and Africa and approximately 5–10 Ma before the creation of the Paraná-Etendeka flood basalts associated with the arrival of the Tristan plume head at the base of the lithosphere. The initial mantle temperature equals an adiabatic profile with a potential temperature of 1613 K. A cold top boundary layer represents continental lithosphere with a temperature of 273 K at the surface, and a half-space cooling age of 60 Ma. For the material parameters discussed in section 2.3, this results in a depth of approximately 130 km for the 1613 K isotherm—an estimate for the initial lithospheric thickness of our model. Throughout the model evolution (from 140 Ma ago to present day), the temperatures and velocities are prescribed at all boundaries to allow the incorporation of constraints from observations and previous modeling studies.

The large-scale flow field on all sides and the bottom of the box is obtained from a global flow model described in section 2.2 and supporting information Text S1. We note that in contrast to, e.g., *Tan et al*. [2006], this is a one-way coupling and there is no feedback from the regional to the global model. Moreover, we use a plate reconstruction described in section 2.2 and supporting information Text S2 to prescribe the plate velocities at the top. We interpolate between these two boundary velocities at the sides of the model to form a gradual transition at the lithosphere-asthenosphere boundary in a depth of approximately 200 km, using a hyperbolic tangent interpolation function. Additionally, the influx of the plume at the bottom of the box is prescribed. At 135 Ma, a spherical temperature perturbation of 300 K and with a radius of 250 km is flowing in, simulating the plume head arriving from the lower mantle. A plume inflow at 135 Ma corresponds to an eruption age of 132 Ma [*Doubrovine et al*., 2012], but the initial starting age of the LIP could also be a few million years older [*Gibson et al*., 2006; *Thiede and Vasconcelos*, 2010; *de Assis Janasi et al*., 2011]. The size is consistent with the LIP volume [*Richards et al*., 1989; *Gladczenko et al*., 1997; *Peate*, 1997; *Courtillot et al*., 1999], estimates of eruptives versus total melts [*Bryan and Ernst*, 2008] and degrees of melting in plume heads [*Katz et al*., 2003], as well as numerical models [*Lin and van Keken*, 2006]. After the arrival of the plume head, a fixed influx of material following a Gaussian distribution with a maximum velocity of 5 cm/yr, a maximum excess temperature of 200 K and a radius of 130 km is added to the global flow velocity, maintaining a stable plume tail. We choose the colder inflow temperature for the plume tail compared to the plume head to be consistent with observations [*Herzberg and Gazel*, 2009]. These parameters result in a plume buoyancy flux of approximately 1000 kg/s, which is in agreement with estimates for the Tristan hotspot as discussed in section 2.4. An important consequence of adding the plume velocity to the global flow field is that the effective plume buoyancy flux is changing over time. For the reference model, this results in an effective flow between 900 and 1250 kg/s.

The plume position is obtained from the global model, which computes the distortion of a plume tail by a combination of buoyant ascent and global mantle flow. This global hotspot motion model is described in supporting information Text S1. However, the hotspot motion model only provides the location where plume material arrives at the base of the lithosphere and not the inflow position in the regional model. Hence, the position of the inflow of plume material at the bottom of the regional model has to be chosen differently for every individual model. We compute this influx position by iterating the regional model with updated inflow positions and comparing plume arrival below the lithosphere to the global hotspot motion model until they are within a distance of less than 500 km of each other. In general, this required up to three iterations of the model. The temperature at the side and bottom boundaries follows an adiabatic profile with a top thermal boundary layer equivalent to an age of 60 million years, roughly corresponding to the present-day age of the sea floor at the positions of the model boundaries. The temperature at the top is fixed to 273 K.

As our velocity boundary conditions are derived from different sources (i.e., plate reconstruction and global convection model) but are integrated into a single model, it is not guaranteed that the overall inflow and outflow of mass is balanced, which would violate the continuity equation. For the purpose of making the equations solvable numerically, this can be fixed by applying a compatibility modification to the right-hand side of equation (1): adding a small constant value to the compressibility, which has the effect of allowing material to be compressed more (or less) for the same pressures, leads to a different net velocity divergence inside of the model. This approach is useful if the net mass inflow/outflow (and hence the correction) is small but will otherwise result in a nonphysical solution. Therefore, an iterative mass flux correction has been applied to all model configurations by computing a first model run with the original velocity boundary condition and then modifying the boundary flux by the integrated inflow/outflow for each time step in a second model iteration. We distributed the correction equally over the asthenosphere and only over the western and eastern boundary—the preferred orientation of flow in the South Atlantic. In all presented models, the correction is usually small—less than 0.5 cm/yr.

2.2. Plate Reconstructions and Large-Scale Mantle Flow

As discussed above, we prescribe plate motions as surface boundary conditions in our models, employing plate reconstructions that are derived and discussed in *Torsvik et al*. [2009]. Between 140 and 126.9 Ma (120 Ma in our simplified reconstruction, where the plate velocities are kept constant for 10 Ma intervals), there are four separate plates (Figure 3): Africa, South America (originally dubbed Amazonia before 126.9 Ma in *Torsvik et al*. [2009]), Parana, and Colorado. Relative, divergent motion between the African and Parana plate

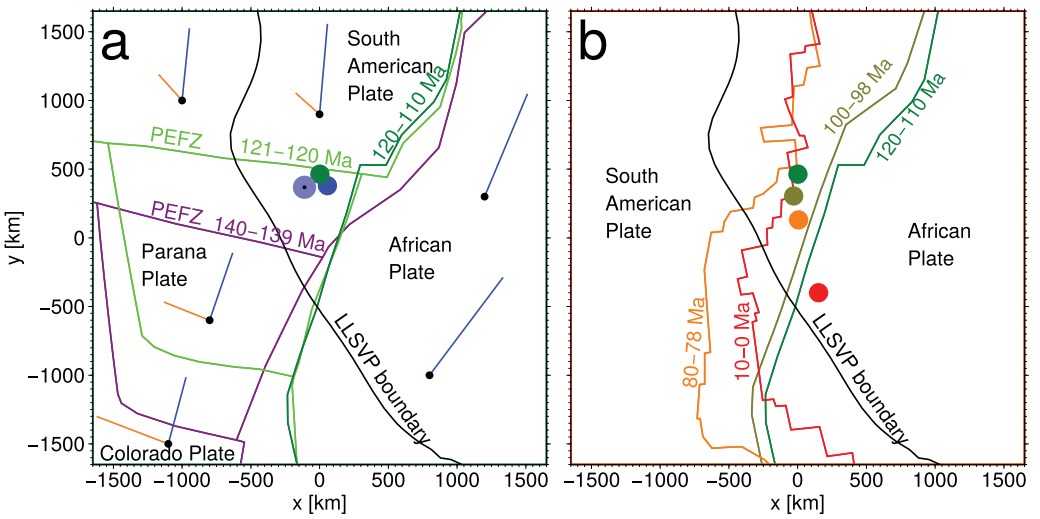

Figure 3. Plate reconstructions updated from *Torsvik et al.* [2010] used as boundary conditions for the geodynamic model for the time periods (a) 140–110 Ma and (b) 110 Ma to present day. (a) Purple line: plate boundaries at 140–139 Ma when relative plate motions began. Bright green line: extrapolated plate boundaries at 121–120 Ma, the final reconstruction with four plates. Dark green line: plate boundary at 120–110 Ma. The total motion between 140 and 120 Ma at selected points on each plate is shown as blue lines, motion relative to the African plate as orange lines. PEFZ = Paraná-Etendeka Fault Zone that became the Florianopolis-Fracture Zone (FFZ) offshore. Also shown are the initial plume location at 132 Ma (blue disk) and the plume location at 120 Ma (green disk). For comparison, the bright blue circle with dot marks the reconstructed eruption center of *Torsvik et al.* [2006] for the Paraná-Etendeka large igneous province in the reconstruction of *Doubrovine et al.* [2012]. However, Paraná flood basalts erupted over a large area on both sides of the PEFZ. The black line marks the boundary of the African LLSVP (1% margin in the SMEAN tomography model [*Becker and Boschi*, 2002] at depth 2800 km). (b) Plate boundaries at 120–110 Ma (green line), 100–98 Ma (olive green line), 80–78 Ma (orange line), and 10–0 Ma (red line). Plume positions at the times 120, 100, 80 Ma, and present day are indicated by green, olive green, orange, and red disks.

is faster than between the African and South American plate. Since extension is symmetric relative to this plate boundary (the future Mid-Atlantic Ridge), the different extension rates imply that an initially straight plate boundary between African plate (east of the boundary), South American plate (west of the boundary in the north), and Parana plate (west of the boundary further south) develops a transform fault east of the triple junction.

This transform fault corresponds to the offshore Florianopolis Fracture Zone, which continues onshore as Paraná-Etendeka Fault Zone (PEFZ) [*Torsvik et al.*, 2009]. In their study, the PEFZ was modeled as a transtensional boundary with a lateral offset of about 175 km. Dextral movements ceased at about 126 Ma and this transtensional zone may have provided upside-down drainage of the Tristan plume explaining the large extent of Paraná volcanism compared to that of Etendeka in Namibia. There is no consensus—from either the surface geology or geophysics data—on the exact localization of intraplate deformation in the South American continent, but the PEFZ is recognized in the free air residual gravity field (e.g., from the GOCE satellite) and in crustal and lithospheric thickness maps [*Braitenberg*, 2015; *Assumpção et al.*, 2013; *Chulick et al.*, 2013].

Another consequence of the different spreading rates is that at 120 Ma, sea floor spreading and the creation of an ocean basin had already begun south of the transform fault, between the African and Parana (and Colorado) plates, while to the north, the plate boundary between the African and South American plate was still in the stage of continental rifting [*Müller et al.*, 2008]. Relative motion of the Colorado/Patagonia plates, further to the southwest, is even slightly faster. However, due to the larger distance, this has little effect on the Tristan plume. Accordingly, our numerical model does not distinguish between the Colorado and Patagonia plates. A detailed description of our regional model of plate motions, and how the transformation from spherical to Cartesian coordinates is done, is given in supporting information Text S2.

The large-scale flow field model used as boundary condition was updated from the one used in *Doubrovine et al.* [2012] as described in supporting information Text S1. Cross sections and map views at 1 and 95 Ma are shown in Figure 4: there is upward flow above the African LLSVP and downward flow related to subduction beneath South America. These are two limbs of a large-scale convection cell, and consequently, in our region of interest, flow is predominantly westward with speeds of several cm/yr, from the upwelling toward

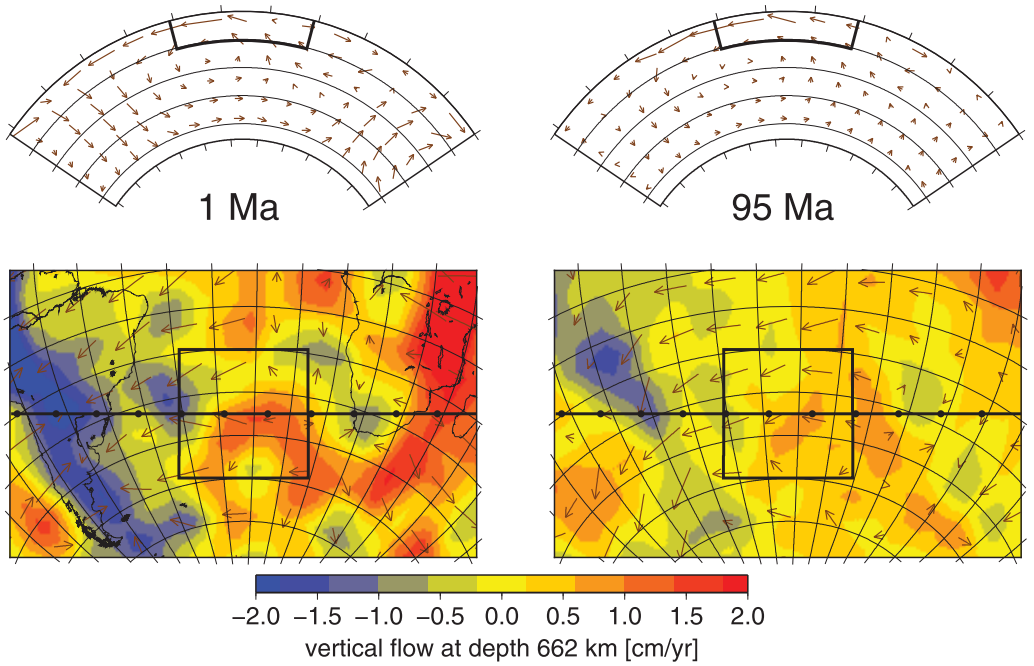

Figure 4. (top) Cross sections and (bottom) map views of the large-scale flow field used as boundary condition for the study area of the high-resolution box model (outlined in black) for times (left) 1 Ma before present and (right) 95 Ma before present. An arrow length of 10° of an arc (at surface in cross sections) is 5 cm/yr, i.e., the length of arrows corresponds to the total amount of displacement in 22.2 Ma (if flow speed was constant). Cross sections are along the profiles in the map below. In the map views, vertical flow (background colors) is shown at the bottom of the box region (depth 662 km), horizontal flow (arrows) at the transition depth between lithospheric and asthenospheric velocities (212 km).

the downwelling. Comparison of the two time intervals shows considerably weaker flow for the earlier time interval: this is an artifact caused by the backward-advection procedure, which leads to an increasing stratification with positive density anomalies near the upper boundary layer and negative ones near the lower one further back in time.

2.3. Numerical Implementation

We use the mantle convection code ASPECT [*Kronbichler et al.*, 2012; *Bangerth et al.*, 2015] that models thermochemical convection in high Rayleigh number flow with adaptive mesh refinement. It solves the equations for the conservation of mass, momentum, and energy. Our models include adiabatic heating, shear heating, latent heat, and take into account mantle compressibility in the limit of the Anelastic Liquid Approximation. Specifically, we consider the following set of equations for velocity **u**, pressure p, and temperature T:

$$-\nabla\cdot\left[2\eta\left(\dot{\varepsilon}(\mathbf{u})-\frac{1}{3}(\nabla\cdot\mathbf{u})\mathbf{1}\right)\right]+\nabla p=\rho\mathbf{g}, \tag{1}$$

$$\nabla\cdot(\rho\mathbf{u})=0, \tag{2}$$

$$\rho C_p\left(\frac{\partial T}{\partial t}+\mathbf{u}\cdot\nabla T\right)-\nabla\cdot k\nabla T=2\eta(\dot{\varepsilon}_s:\dot{\varepsilon}_s)+\alpha T(\mathbf{u}\cdot\nabla p)+\rho T\Delta S\frac{DF}{Dt}, \tag{3}$$

where η is the viscosity, $\dot{\varepsilon}(\mathbf{u})=\frac{1}{2}(\nabla\mathbf{u}+\nabla\mathbf{u}^T)$ is the strain rate, ρ is the density, **g** is the gravity, C_p is the specific heat capacity, t is time, k is thermal conductivity, $\dot{\varepsilon}_s=\dot{\varepsilon}(\mathbf{u})-\frac{1}{3}(\nabla\cdot\mathbf{u})\mathbf{1}$ is the shear strain rate, α is the

thermal expansivity, ΔS is the entropy change across the solid-melt phase transition for peridotite, and F is the melting function.

The radial structure of the viscosity $\eta(z, T)$ in the box [*Steinberger and Calderwood*, 2006] is the same as was used to compute the large-scale mantle flow field used as a boundary condition, but additionally lateral variations—derived from the same temperature dependence of viscosity that was used to compute the radial variations—are considered:

$$\eta(z,T)=\eta_r(z)\exp\left(-\frac{H(z)(T-T_{\mathrm{adi}}(z))}{nRTT_{\mathrm{adi}}(z)}\right). \tag{4}$$

Here $H(z)$ corresponds to a depth-dependent activation enthalpy of the temperature dependence of viscosity as described in *Steinberger and Calderwood* [2006] and ranges from 500 to 700 kJ/mol; n denotes the stress exponent and is set to 3 for the upper mantle, and R is the gas constant. $T_{adi}(z)$ denotes the adiabatic temperature profile. This formulation results in a viscosity change of approximately a factor of 2 over a temperature range of 100 K or a factor of 4 between plume material and surrounding asthenosphere for typical upper mantle temperatures (see supporting information Figure S1 for representative maps and profiles). Because the temperature dependence already introduces a high-viscosity boundary layer at the top, we modified the radial viscosity profile $\eta_r(z)$ to be constant upward of 200 km depth.

The other material parameters, or more specifically, the density ρ, specific heat C_p, and thermal expansivity α are computed as a function of depth and temperature using the thermodynamic calculation package Perple_X [*Connolly*, 2005], a published database for mineral properties [*Stixrude and Lithgow-Bertelloni*, 2011], and assuming a pyrolitic composition [*Ringwood and Irifune*, 1988]. The thermal conductivity k is assumed to be constant at 4.7 W/mK.

We employ a melting parametrization for equilibrium batch melting of anhydrous peridotite [*Katz et al.*, 2003] to compute how much melt is generated in dependence of temperature and pressure during the model evolution. As this melting function $F(p, T)$ considers the change in productivity after the exhaustion of clinopyroxene, it is kinked. The transition from the solid to the melt phase is incorporated in the energy equation as a heat consuming process in the following way:

$$\Delta S\frac{DF}{Dt}=\Delta S\frac{\partial F}{\partial T}\left(\frac{\partial T}{\partial t}+\mathbf{u}\cdot\nabla T\right)+\Delta S\frac{\partial F}{\partial p}\mathbf{u}\cdot\nabla p, \tag{5}$$

where the variables are named as described above. The temperature and pressure derivatives of the melting function $\partial F/\partial T$ and $\partial F/\partial p$ are computed analytically. As melting of mantle rock consumes energy, this leads to a colder mantle adiabat than without the consideration of latent heat effects. For a more detailed derivation of the equations, we refer the reader to the ASPECT manual [*Bangerth et al.*, 2015].

We then use two different methods to track where the melt moves in our model and compute maps of crustal thickness: (1) melt is passively advected with the mantle flow as a field F_{max}, the maximum degree of melting in every point:

$$\frac{\partial F_{\mathrm{max}}}{\partial t}+\mathbf{u}\cdot\nabla F_{\mathrm{max}}=Q$$
$$\text{with } Q=\begin{cases}0 & \text{if } F(p,T)\le F_{\mathrm{max}}\\ (F-F_{\mathrm{max}})/\Delta t & \text{if } F(p,T)>F_{\mathrm{max}}\end{cases}. \tag{6}$$

The crustal thickness at every point in time is calculated by vertically integrating this quantity from the surface up to a depth of 200 km. (2) Alternatively, generated melt is extracted instantly, added up to yield a crustal thickness and advected with the prescribed plate motions at the top of the model. We emphasize that both methods are implemented as purely passive postprocessing steps. Except for the consumption and release of latent heat upon melting and refreezing of melt, the equations (1)–(3) remain unaffected by the melting process. Both techniques are approximations and represent end-member regimes of how we imagine melt migration in the Earth: a combination of porous flow in the mantle and fast ascent through channels and dikes in the lithosphere (see also supporting information Text S3). However, modeling two-

Table 1. Model Configurations[a]

Model	Plume Position	Inflow ΔT (K)	Inflow Velocity (cm yr^{-1})	Inflow Radius (km)	Buoyancy Flux (kg s^{-1})
Reference	Reference (see Figure 3)	200	5.0	130	950
East150	150 km east of reference at 132 Ma	200	5.0	130	950
East300	300 km east of reference at 132 Ma	200	5.0	130	950
$\Delta T150$	Reference	150	3.75	130	700
$\Delta T250$	Reference	250	6.25	130	1500
Flux500	Reference	200	3.61	110	500
Flux1700	Reference	200	6.66	150	1700
ThinLith	Reference	200	5.0	130	950
ThickLith	Reference	200	5.0	130	950
RealLithC1	Reference	200	5.0	130	950
RealLithC2	Reference	200	5.0	130	950
NoGlobalFlow	Reference	200	5.0	130	950
NoPlume					0.0
RefShift	Track toward Gough Island	200	5.0	130	950
Track2	*Steinberger et al.* [2004]	200	5.0	130	950
Track3	Modified *Steinberger et al.* [2004]	200	5.0	130	950

[a]Excess temperature ΔT, inflow velocity v, and inflow area $A = \pi R^2$ were varied to be consistent with Stokes' law for the rising/sinking velocity in a viscous medium: $\Delta T A v^{-1} = \text{const}$.

phase flow in three dimensions and on long time scales is extremely challenging and outside the scope of this paper. Thus, we will show crustal thickness maps generated with both approximations and indicate which method was used in the respective figure captions.

We utilize ASPECT's adaptive mesh refinement to refine regions with high-temperature gradients in the lithosphere and in the rising plume. Although we are mostly interested in the region close to the plume and the ridge, the passive advection approach for crustal thickness described above makes it necessary to refine the whole model domain above 200 km depth. The minimal mesh cell size is set to approximately 20 km, which would generate a mesh of 160 × 160 × 32 elements for a uniform resolution, resulting in 34 million degrees of freedom. Adaptively reducing the resolution in the asthenosphere and transition zone outside the plume region decreases this to 15 million degrees of freedom for the presented models. The use of quadratic finite elements for temperature and composition as well as second-order velocity and first-order pressure elements (Q2Q1) for the Stokes system allows for higher accuracy compared to the commonly used linear elements, and for a distance between quadrature points of around 10 km. The timespan of 140 Ma is divided into approximately 3100 BDF-2 time steps (second-order backward differentiation formula) [see *Kronbichler et al.*, 2012], which are iteratively solved on average 2 times to account for nonlinearities in the equations (e.g., due to latent heat). This corresponds to 6200 solves of the coupled Stokes-advection system. An average model run on 768 Xeon E5-2860v3 cores at 2.5 GHz takes 16 h and therefore consumes 12,500 core hours.

2.4. Variation of Model Parameters

We ran a series of models with different plume inflow positions, temperatures, and buoyancy fluxes to investigate their respective influence on the evolution of the Tristan hotspot track, the distribution of associated melting events, and the thickness of the generated oceanic crust. For this purpose, we varied these model parameters within the bounds of the uncertainty of the relevant observations and reconstructions (see Table 1 for a list of model setups):

1. The excess temperature of the plume tail at the bottom boundary of the model is varied between 150 and 250 K, with 200 K being the value used in the reference model. As the plume ascends, it loses heat to the surroundings, so that the temperature upon melting is approximately 40 K lower than the maximum inflow temperature. Taking into account this cooling process, the chosen plume temperatures are consistent with estimates for excess temperatures of hotspots in general (100–250 K) [*Herzberg and Gazel*, 2009] and the Tristan hotspot track in particular (100–180 K) [*Herzberg and Asimow*, 2008; *Schilling*, 1991; *Putirka*, 2008].

   For varying model parameters between different model configurations, we have to make sure that we retain the consistency of the inflow velocity with the plume velocity inside of the model. Hence, we

change the plume excess temperature ΔT, the inflow velocity v, and the inflow area $A = \pi R^2$ together, such that $\Delta T A v^{-1} = \text{const}$. This equation follows from Stokes' law for the rising/sinking velocity of a sphere in a viscous medium.

2. The setup adapted from *Doubrovine et al*. [2012] as described in section 2.1 implies a plume buoyancy flux of approximately 1000 kg s^{-1} as estimated inflow from the lower mantle. However, these estimates vary and are not well constrained. Additionally, plume fluxes may be considerably larger, if plumes primarily feed into the asthenosphere as suggested by *Morgan et al*. [2013]. In this case, only a small fraction of the total anomalous mass flux is represented by the swell. Accordingly, we vary the plume flux in our model in the range of published estimates from 500 kg s^{-1} [*Davies*, 1988] to 1700 kg s^{-1} [*Sleep*, 1990]. For this purpose—following the same principle as mentioned under (1)—we change the inflow area and velocity while keeping the plume temperature constant.
3. Our computed hotspot motion model is described in section 3.1. We use this as a reference case, but also move the position of the arriving plume from the lower mantle 150 and 300 km to the east: the *Doubrovine et al*. [2012] reference frame only goes back to 124 Ma, before that there are no strong longitude constraints of plume position relative to the plates because of the large extent of flood basalts. A 300 km shift from 132 to 124 Ma corresponds to ≈4 cm/yr additional eastward plate motion, which is not unreasonably fast. Additionally, we employ an alternative hotspot motion model based on *Steinberger et al*. [2004]. This model also implies a different absolute plate motion reference frame, hence different plate boundary locations through time. However, here we do not modify plate boundary locations and instead modify the hotspot motion such that the relative location of hotspot and plate boundary remains the same. Last, variations of both this motion model and the reference model are tested, where the youngest part of the plume track is adjusted to end under Gough Island instead of the middle between Tristan and Gough Island.
4. We varied the initial thickness of the lithosphere to test its influence on the spreading plume head and large igneous province generation. The variations range from a lithosphere half-space cooling age of 40–100 Ma, resulting in 1613 K isotherm depths of 110–160 km. In addition, we also used more realistic lithosphere models as described in supporting information Text S4. These models prescribe a spatially variable lithospheric thickness, derived from the present-day lithosphere structure as seen in seismic tomography models, and then moved backward in time using the plate reconstruction of our reference model.
5. We evaluate the influence of the prescribed large-scale flow field on the plume shape and evolution by computing models with no inflow and outflow of material (no-slip boundaries) except for the plume influx, the lithospheric plates, and the correction to balance the net mass flux as described in section 2.1. We then compare the results of this model to our reference model with prescribed boundary velocities derived from a global mantle convection model. During this comparison, we take into account that the global velocities lead to some additional plume buoyancy flux and therefore the effective averaged buoyancy flux in the model without global flow is lower by 200 kg/s compared to the reference model.

3. Results

3.1. The Hotspot Motion Model: Geometrical Relation of Plume and Ridge

Before discussing numerical model results, we describe the relative location of plume and ridge in terms of on-ridge and off-ridge track in order to get a first qualitative understanding of the effect of plume-ridge interaction on hotspot tracks.

As a first step, we adopted the plume motion model of *Doubrovine et al*. [2012] as described in supporting information Text S1. The modeled plume positions in the reference case for selected times are shown in Figure 3 together with the plate reconstruction. The initial plume head erupts beneath the South American (Amazonian) plate and near the Paraná-Etendeka Fault Zone (PEFZ). Due to northward plate motion and the opening of the South Atlantic, the plume was located south of the transform fault that corresponds to the Florianopolis Fracture Zone after approximately 120 Ma. Subsequently, sometime between 100 and 80 Ma, the plume was overridden by the ridge and has been beneath the African plate since then.

Using this plume motion model and the plate reconstruction described in section 2.2, we can generate a map illustrating ocean floor ages and plume track geometry (Figure 5a). The latter is computed by projecting the predicted plume position to the surface and kinematically advecting it with the plate velocities to

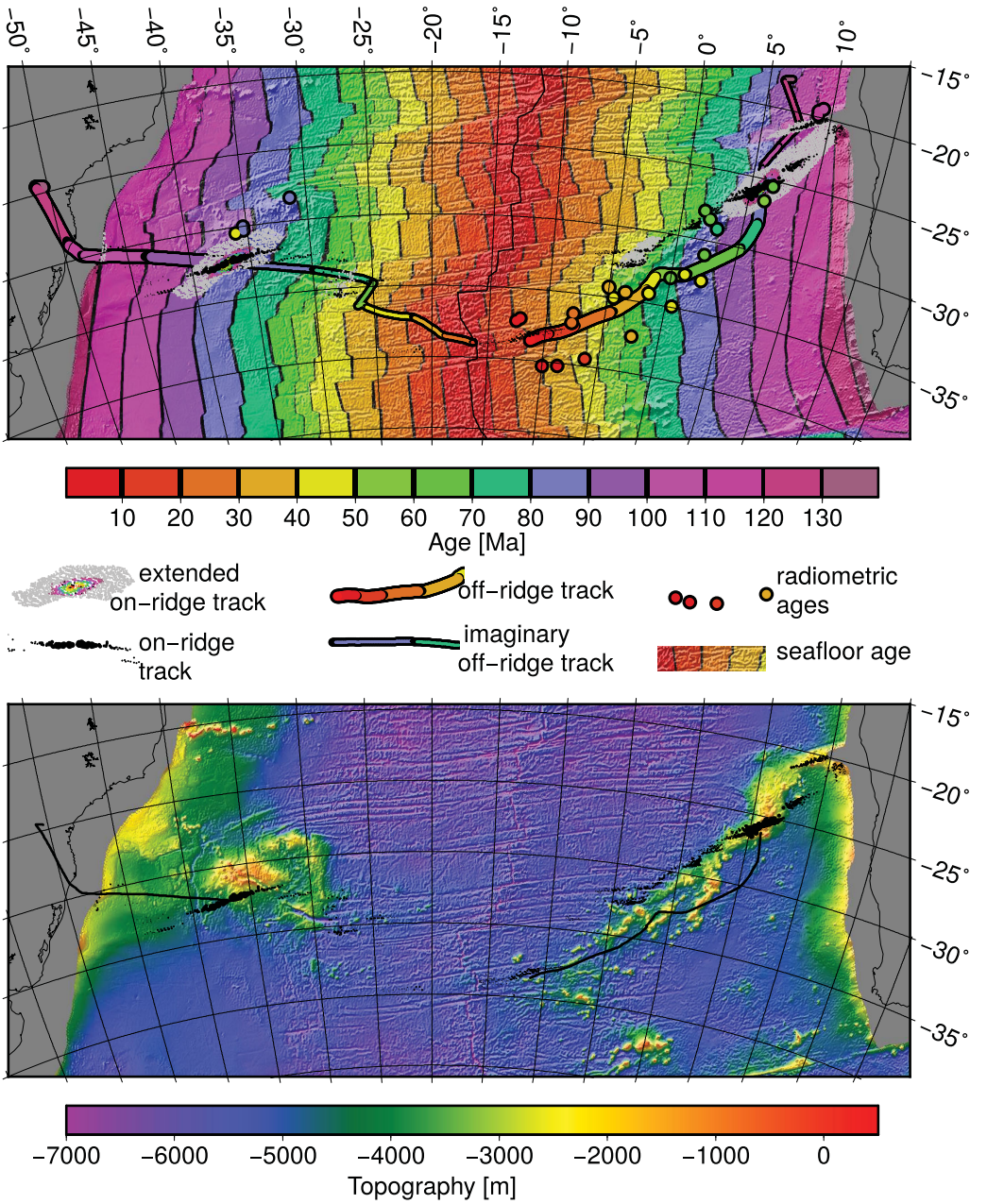

Figure 5. (top) Computed Tristan hotspot track for the model of *Doubrovine et al*. [2012] relative to the South American and the African plate. Also plotted on the same color scale is the ocean floor age grid of *Müller et al*. [2008] and a compilation of radiometric seamount ages from *O'Connor and Duncan* [1990], *O'Connor and le Roex* [1992], *Rohde et al*. [2013], *O'Connor and Jokat* [2015b], and references cited therein (circles). The thick colored line is the off-ridge track (classical hotspot track), thin colored lines are imaginary tracks computed from plate and hotspot motions (with ages older than sea floor age). Black dots show the "on-ridge track" (ocean floor generated on the ridge segment closest to the hotspot) if the distance is less than 500 km (dot size inversely proportional to distance if greater than 100 km and constant if less than 100 km) and colored dots surrounded by gray dots show the "extended on-ridge track" (all ocean floor generated at a distance of less than 300 km from the hotspot; colored dots if distance less than 140 km, same color scale for distance [km] as age [Ma]). (bottom) Topography, corrected for the ridge by subtracting $330\,\mathrm{m} \cdot (\sqrt{\mathrm{age[Ma]}} - 10)$ for sea floor ages less than 100 Ma for comparison (residual topography).

create a hotspot track. This also allows us to calculate the distance between the closest ridge segment and the plume-arrival position, making it possible to differentiate between on-ridge and off-ridge tracks.

Technically, an off-ridge track can only occur with hotspot age younger than sea floor age (thick colored line). But one can imagine that the spreading ridge had been at a different location, such that the plume had been beneath the plate on the opposite side of the ridge. The imaginary off-ridge tracks that result

from this thought experiment—with ages older than sea floor age (given the true ridge location)—are shown as thin colored lines and are still useful for estimating plume-ridge distance by comparing the colors of the off-ridge track and the background sea floor. If plume and ridge are sufficiently close to each other, volcanism may also occur on nearby ridge segments, leading to thickened crust on both sides of the ridge. The colored centers of the gray, roughly elliptical areas (called "extended on-ridge track" in Figure 5, top) mark the sea floor where the hotspot crossed from the South American to the African plate at 90 Ma. The part of the ocean floor generated within less than 300 km of the hotspot approximately corresponds to the Rio Grande Rise and the part of the Walvis Ridge with most pronounced topography. After this time, the "on-ridge track" generated on the African plate at the ridge location closest to the hotspot resembles the northwesternmost chain of seamounts within the Walvis Ridge. Figure 5 shows that our hotspot motion model does not always coincide with the observed volcanic chain. This already indicates that plume-ridge interaction must play a crucial role in determining the melt distribution—an effect we will quantify in the following sections about the dynamic models.

3.2. Time Evolution

3.2.1. Large Igneous Province and Opening of the Rift

Our interpretation of the high-resolution geodynamic model of the South Atlantic region is structured into two main parts: we first describe the evolution of the reference model in detail, compare it to observations and analyze the occurring physical processes. The model evolution, including melting processes and generated crustal thickness, is shown in supporting information Movie S1. In a second step, we describe the effects of varying essential input parameters as outlined in section 2.4.

We begin the evolution of the reference model at 140 Ma before present day (see also supporting information Movie 1). The model starts with a uniform lithospheric thickness and prescribed divergent plate motions that thin the lithosphere at the plate boundary and later initiate the rifting. At 136.25–135 Ma, we prescribe the influx of the plume head at the lower boundary of the model, which corresponds to the arrival of the Tristan plume head at the boundary between upper and lower mantle. From there, the plume rises and approaches the base of the lithosphere of the South American plate, causing the first melt generation at 134 million years. As the plume head spreads laterally, the melt production increases, reaching a maximum crustal thickness of 4 km above the center of the plume with decreasing thickness toward the edges within 3 million years. The maximum diameter of the melting region is 900 km, which agrees well with estimated areal extensions of the Paraná-Etendeka LIP ($1.5–2 \times 10^6$ km^2) [*Richards et al*., 1989; *Peate*, 1997; *Courtillot et al*., 1999].

At 131 Ma, the plume has generated a total melt volume of 10^6 km^3. Considering that the intrusive or underplated magma volume can be up to 10 times larger than the associated extrusive volume [*Bryan and Ernst*, 2008], this volume is significantly lower than what is expected for the Paraná-Etendeka flood basalts (1×10^6 to 2.35×10^6 km^3) [*Richards et al*., 1989; *Gladczenko et al*., 1997; *Peate*, 1997; *Courtillot et al*., 1999]. The most plausible explanation for this deviation is that we do not consider thermomagmatic erosion of the lithosphere in our models, which is known to lead to thinning of the lithosphere, increasing melt generation enormously [*Sobolev et al*., 2011]. At 128 Ma, the plume head has generated the majority of its melt and it has cooled and dissipated a part of its heat so that the melt generation is restricted to three regions: (1) a narrow plume tail with a diameter of 100 km, (2) a 50 km thick ring of minor melting in the spreading outer regions of the plume head, where material is still upwelling and that only grows until 126 Ma and then fades until 121 Ma, and (3) the regions with thinner lithosphere southeast of the plume center where the rift begins to open.

Apart from the plume-influenced region around the FFZ, the first purely rift-related melts are generated at 128 Ma in the southernmost part of the rift, where it opens first. From there, the melting region propagates northward until it reaches the Florianopolis Fracture Zone at 124 Ma. This opening process is strongly influenced by the plume head intruding into the rift around the FFZ and generating melt, which starts at 130 Ma and reaches its maximum melt production at 122 Ma, leading to a crustal thickness of up to 19 km. We emphasize that at this time the plume tail reaches the base of the lithosphere around 260 km northwest of the zone of maximum melt production and most of its material flows northwestward with the plate (only a small amount intrudes into the landward PEFZ). Therefore, the majority of the additional decompression melting in the rift is caused by the older but still hot plume head material that now ascends into the

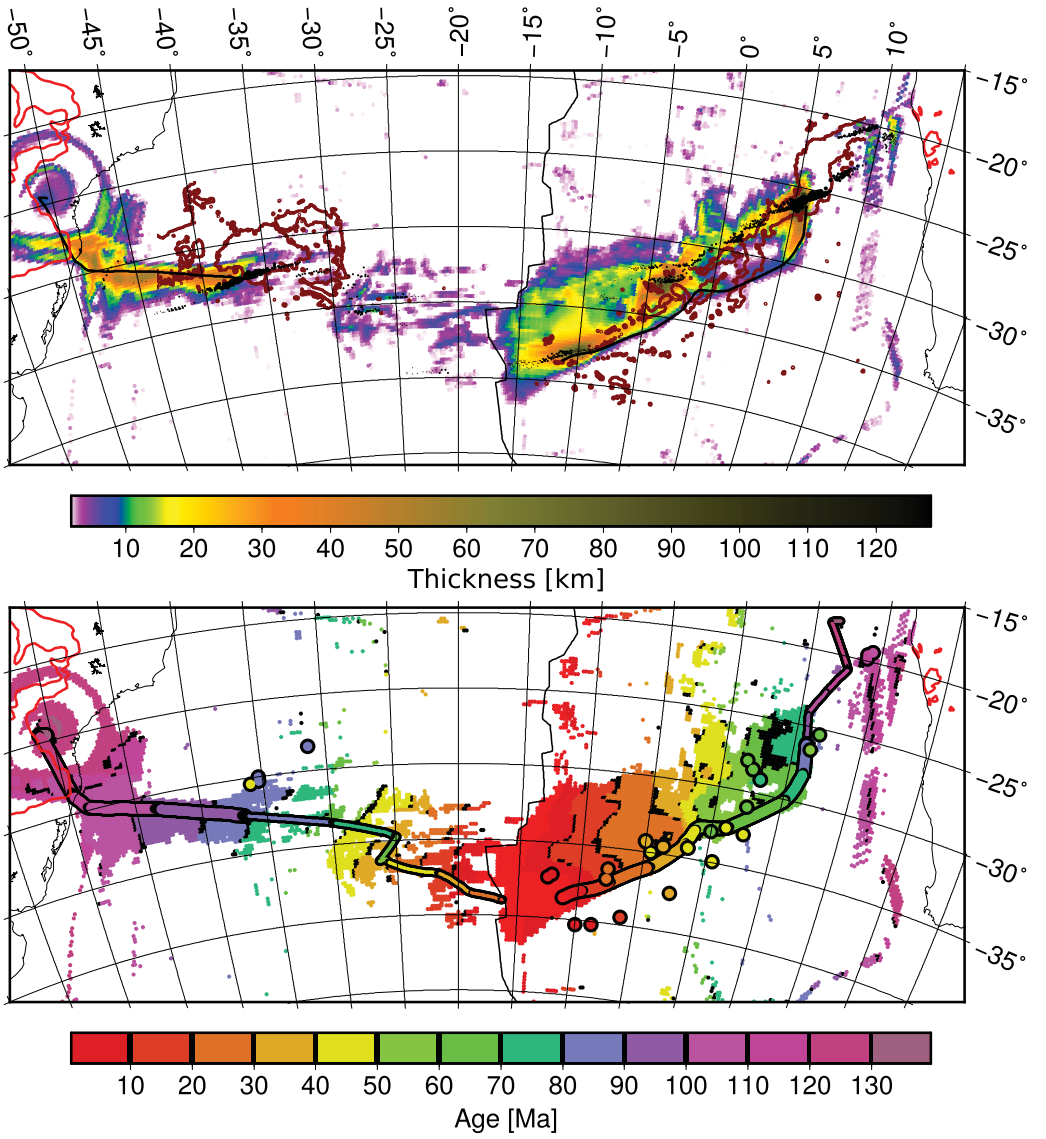

Figure 6. (top) Plume-generated crust in the reference model at the present-day state, computed as the difference between models with and without plume. Also shown are the assumed off-ridge track (continuous black line) and on-ridge track (dots, as in Figure 5, top) for comparison. The observed hotspot track is represented by dark red contours (often only appearing as isolated dots) of −3700 m ridge-corrected topography (as in Figure 5, bottom). LIP outlines are shown on land in bright red. (bottom) Age of the additional crust (youngest layer with thickness larger than 50 m generated in a 0.25 million year time interval). Thin and thick colored lines and colored dots are as in Figure 5, top. Both plots can be directly compared to Figure 5 and crustal thickness is tracked by instant melt extraction and advection with the plate velocities.

opening rift. The part of the rift north of the fracture zone opens later at 118 Ma and is largely unaffected by the plume head material. In our model, the average oceanic crustal thickness without plume influence amounts to 5–7 km—depending on the spreading rate—which agrees well with observations in this region [*Fromm et al*., 2015].

3.2.2. Plume Shape in Dependence of Its Position Relative to the Ridge

While the plume tail is still reaching the surface west of the rift, it generates a hotspot track with a maximum crustal thickness of 21 km (up to ≈60 km plume-generated crust along a narrower track, if melts are tracked with plate motions; Figure 6), and the maximum melt fraction inside the plume is approximately 28%. The melting region is influenced by the fast movement of the South American plate, shaping it to a fan elongated in the direction of the plate motion (supporting information Movie 1, at 95 Ma). Once the plume reaches the rift at approximately 90 Ma, it is focused to a thin column and melting is concentrated at the ridge. In the following 10 Ma, the plume tail and the African plate move eastward with approximately

the same speed so that their positions relative to each other are unaffected. The melting region remains close to the ridge and broadens, leading to a high melt production and a calculated plume-generated crustal thickness even exceeding 100 km in a small area (Figure 6, 5° E 27°S). Such thick crust is at odds with observations and we refer to section 4 for a discussion of mechanisms that could reduce melt generation when the plume crosses the ridge. At 70–60 Ma, the plume tail starts to move south, and the African plate accelerates, with the South American plate also changing its absolute movement direction from westward to eastward. The associated change in the global flow field leads to a fast movement of the upper part of the plume away from the ridge, shaping it to a shallow, thin pancake with a maximum melt fraction of less than 15%, and a lower additional crustal thickness of less than 10 km. At 60 Ma, the African plate changes direction again, moving toward the southeast, and at 50 Ma also the South American plate begins to move westward again. This draws the upper part of the plume back to the ridge, whereas between 40 and 30 Ma, when the African plate moves faster again, the plume straightens up again, changing its shape back to a columnar structure. This cycle is repeated as the plume accelerates southward relative to the plate between 30 and 10 Ma, slowly tilting toward the ridge again. It then remains more or less constant in place until present day.

In general, thicker crust is produced when the global mantle flow favors a stable plume tail and melting region relative to the plate, while the plume forms a flat pancake and produces less additional crust while it moves relative to the plate. Additionally, a faster plate movement drags the plume away from the ridge, and therefore not only the lateral motion of the plume tail but also the distance between plume track and ridge is correlated with the speed of the African plate. This distance, however, also controls the age and thickness of the overlying lithosphere. Hence, the amount of generated crust is anticorrelated with the distance between plume track and ridge (shown by the distance between off-ridge and on-ridge track in Figure 6). Regions where the plume reaches the lithosphere close to the ridge like 5°E, 4°W, and 10°W have much higher crustal thickness than regions with a larger distance at 0° and 7°W. For the full time evolution of the model, we refer to supporting information Movie 1 and a more detailed visualization of the crustal production in dependence of the distance to the ridge is shown in supporting information Movie S2.

3.3. Present-Day Crustal Thickness Distribution and Influence of Hotspot Motion Model

From the model evolution described in section 3.2, we compute crustal thickness and age maps by extracting all generated melt to the surface immediately and moving it with the plate velocities (Figure 6). We then compare the modeled crustal thickness to the residual topography of the South Atlantic region (Figure 5, bottom), assuming that the topography strongly correlates with the crustal thickness. We start with the oldest part of the hotspot track and progress in time toward the present day.

The general pattern of thickened crust in our model resembles observations in the South Atlantic. On the South American margin, the position and age of the generated crust agrees with the observed hotspot track and the Rio Grande Rise. After the plume jumps to the African side of the ridge, it generates several segments of the hotspot track with varying width and thickness, depending on the proximity to the ridge (black dots in Figure 6, top mark the on-ridge track of the hotspot) and speed of the African plate, as discussed in section 3.2.2. Overall, these segments correspond to topographic features of the Walvis Ridge. Examples are the broad regions of thickened oceanic crust at the beginning of the track at 5°E and between 0° and 5°W, and the narrow segment at 0°–5°E.

In the youngest part of the hotspot track, our models show a steep slope from thickened crust to "normal" ocean floor toward the south, but a more gradual transition toward the north and west, where the mid-ocean ridge lies. The smooth transition is caused by the channeling of plume material that arrives at the base of the lithosphere toward the ridge, which leads not only to a lateral movement but also to a slow ascent while the lithosphere gradually decreases in thickness toward the ridge. This process allows additional melt to be generated between the primary melting regions at the hotspot track and the mid-ocean ridge, especially in regions where the lithosphere is thinned by transform faults. It leads to the development of a broad region of thickened crust with a width of up to 500 km. Moreover, this mechanism provides an explanation for the observations of *O'Connor and Jokat* [2015a], who find that the south-eastward transition between Walvis Ridge and Cape Basin is much more abrupt than the smoother transition to the Angola Basin in the northwest.

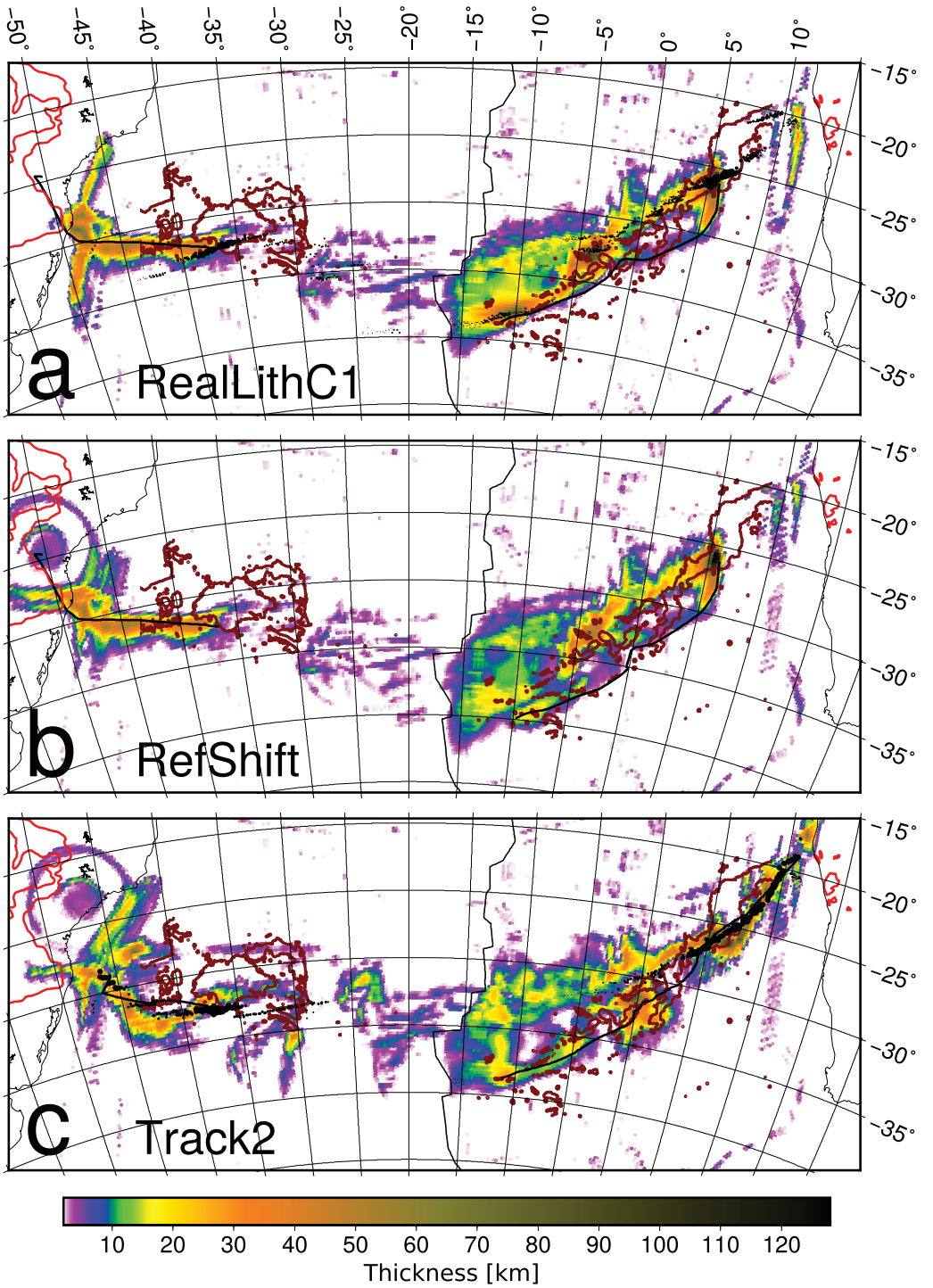

Figure 7. Plume-generated crust (melt advected with plate motions) at the present-day state for the three model cases RealLithC1, RefShift, and Track2. Other features shown as in Figure 6.

Employing variations of the hotspot motion model (as described in section 2.4) to compute the plume position, reveals that in some models two parallel lines of volcanism with similar ages are generated (like Figures 7b and 7c). These lines approximately correspond to the observed Tristan and Gough volcanic chains. Figure 6, top and Figure 7 also show that these two tracks represent a separation of the off-ridge track (directly above the plume, continuous black lines in the figures) and the on-ridge track (at the ridge, closest to the hotspot, black dots in the figures). The areal extent of the region where melt is generated at

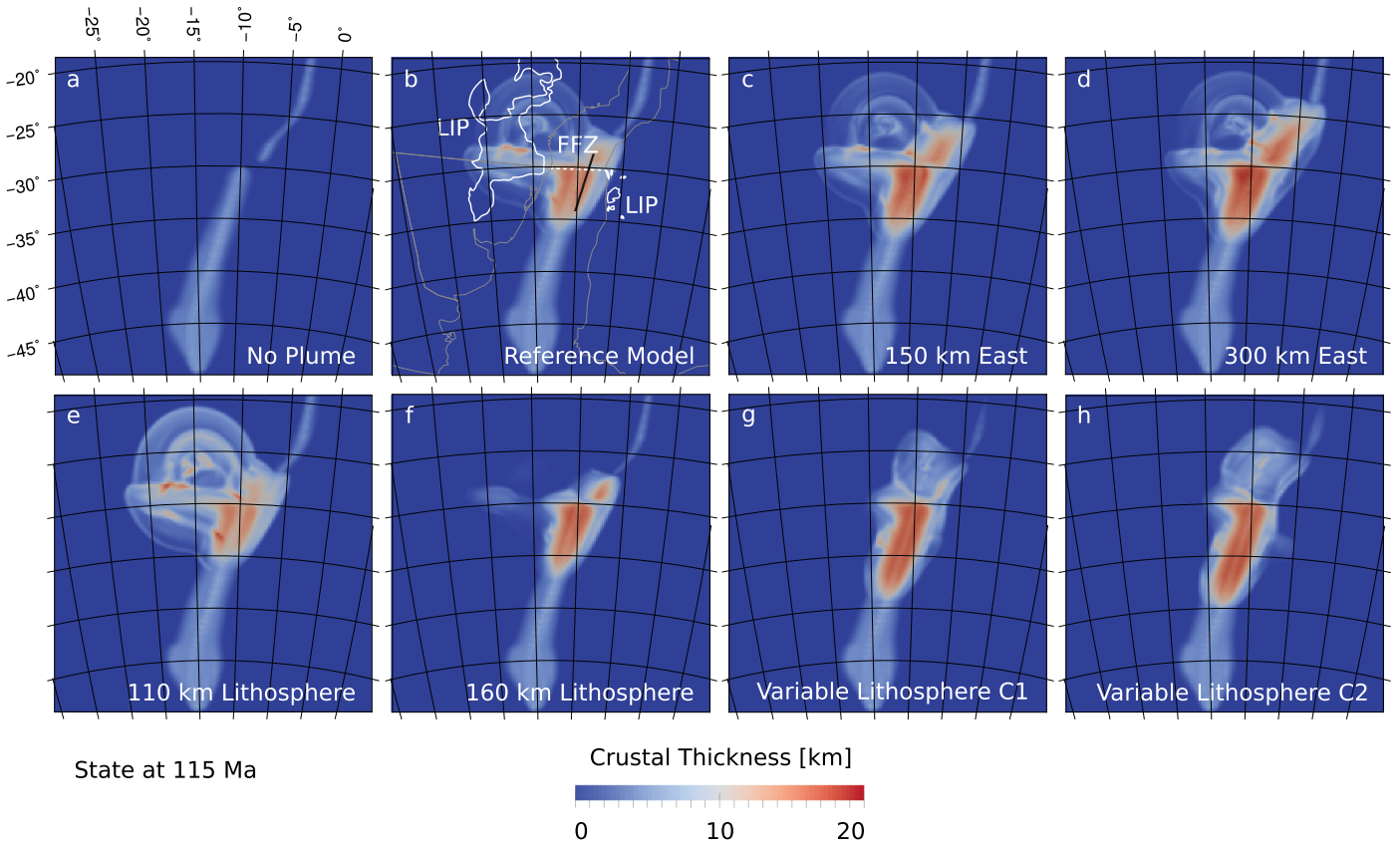

Figure 8. Computed crustal thickness distribution in the rifting and post-rift phase at 115 Ma for (b–d) different initial plume head positions and (e–h) lithosphere properties. The top row displays (a) a model without plume, (b) the reference case, and a plume head that is shifted eastward by (c) 150 km and (d) 300 km, respectively, compared to the initial reconstruction of the hotspot track. The bottom row features models with a lithosphere thickness that is reduced to (e) 110 km, increased to (f) 160 km, or prescribed according to (g, h) two different more realistic lithosphere models described in supporting information Text S4, with (h) featuring stronger lithospheric thickness variations. In addition, Figure 8b includes the outlines of the continents and former plate boundaries (gray lines) and the Paraná-Etendeka LIP [*Coffin et al*., 2006, white line], the position of the FFZ (dashed line) and the crustal thickness profile shown in supporting information Figure S3 (solid black line), all reconstructed to their 115 Ma location. Crustal thickness is computed by passive advection of melt.

any given time (supporting information Movie S2) is broadly similar to the observed spread of volcanism with similar radiometric age (supporting information Figure S2) —about 5° in longitude.

Multiple parallel tracks or one broad track are generated mainly when the plume was in an intraplate location on the African plate: after it was at the ridge at ≈90 Ma (creating thick crust now around 5°E 27°S in the reference case) and started to move away, on-ridge volcanism was dominant. Hence, the single track observed between ≈5°E 27°S and 3°E 29°S in a similar location to our model track could be an on-ridge track, whereas during that time the off-ridge track directly above the hotspot could be entirely absent.

3.4. Plume Head Position and Postrift Ocean Floor Thickness

In addition to analyzing the model evolution in general and comparing it to the present-day South Atlantic, we vary the position of the modeled plume head and the thickness of the lithosphere as described in section 2.4. We then investigate under which conditions our model reproduces the observed LIP magmatism associated with the Tristan plume head and if that allows us to constrain the plume head properties. To quantify the spatial pattern and volume of melt generation, we also compute a model without plume and identify the region where melt is produced. We define melt generated within this region in all models as purely rift-associated melts, but melt generated outside this region in the presence of a plume as LIP-associated melts that are attributed to their respective continents. We here only take into account melt accumulated in the first 20 Ma after the plume reaches the surface (equivalent to 135–115 Ma).

All models that include a plume predict melting where the plume head impinges on the lithosphere, and at the PEFZ and FFZ, as well as increased melt generation at the mid-ocean ridge compared to a model without plume influence (Figure 8). Moreover, the generated oceanic crust is significantly thicker directly south

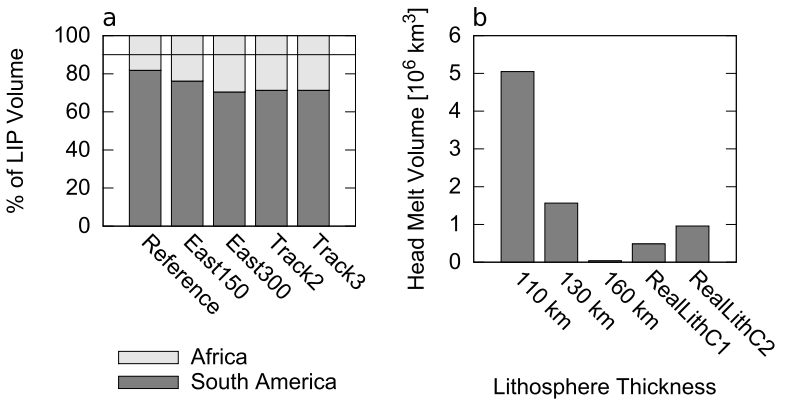

Figure 9. (a) Volume distribution of plume-related melts at 115 Ma for different plume positions. East150 and East300 shift the plume head by 150 and 300 km, respectively, and Track2 uses an alternative hotspot motion model by *Steinberger et al*. [2004]. Track3 is a modified version of Track2 as described in section 2.4. The overall melt volume is approximately 5.5×10^6 km^3 for all models. The black line marks the observed distribution of flood basalts between the Paraná and Etendeka provinces [*Peate*, 1997]. (b) Total melt volume generated by the plume head in dependence of the initial lithosphere thickness in the model. The two models RealLithC1 and RealLithC2 shown in the last two columns are initialized with variable lithosphere models that are derived from today's lithosphere thickness rotated back to the beginning of the model runtime, see supporting information Text S4 for details. All melt volumes are computed by passive advection of melt.

of the FFZ, where the rift opens first. The amount of melt generated north of the FFZ is much smaller, as the plume head has cooled once the spreading begins in this area. For a detailed comparison between our models and a seismic profile, we refer to supporting information Text S5 and supporting information Figure S3.

An eastward shift of the plume head by 150 km respectively 300 km only changes the east/west distribution of the generated melt by less than 5% of the total volume. The majority of more than 75% of the melt is still produced on the South American side (Figures 9a, 8b–8d). Presumably only an arrival at the African side of the rift would lead to a significantly larger amount of melt produced there. The same is true for computations employing different models of the hotspot track (Figures 7b, 7c, and 9a, Track2 and Track3). However, all presented models agree with the observed melt distribution of the Paraná-Etendeka LIP, for which up to 90% of the magmatic volume is observed on the South American side [*Richards et al*., 1989]. *Becker et al*. [2014] pointed out that this pattern is at odds with the distribution of possibly magmatically underplated crust below the continental margin, which is between 1.5 and 3 times more voluminous in Africa compared to South America. Hence, we conclude that the LIP distribution can be explained by a plume head arriving mainly below South America, but the thicker African margin might be more easily explained by processes not covered in our model, such as asymmetric rifting [*Brune et al*., 2014]. This also implies that our models do not allow us to further constrain the position of the plume head arrival.

The initial thickness of the lithosphere, on the other hand, has an important influence on the accumulated melt volume the plume head produces below the continents. While a thin lithosphere of 110 km increases the amount of plume-related melts by a factor of 3 in comparison to the reference of 130 km, a 160 km thick lithosphere leads to virtually no melt being generated apart from the mid-ocean ridge (Figure 9b). The models using lithospheric thickness models derived from seismic tomography and plate motions (RealLithC1 and C2, see supporting information Figure S4 and supporting information Text S4) generate a similar crustal volume as the reference model but feature a different melt distribution (Figures 8g and 8h). Due to the large contrast between the thick continental lithosphere of approximately 250 km and the only 80 km thin lithosphere close to the future rift, melt is focused toward the rift, resulting in a more elongated shape of the produced thickened magmatic crust. Considering the increased but still minor melt generation on the African side of the rift especially lithosphere model C2 creates a more realistic pattern for the Etendeka LIP (Figure 8h, 7°W, 33°S). However, due to a thicker lithosphere in the region of the PEFZ on the South American side, it does not reproduce the large westward extent of the Paraná LIP.

These results demonstrate how important the properties of the overlying lithosphere are for the spatial extent and distribution of large igneous provinces. Despite its more realistic approach, the overall thickness

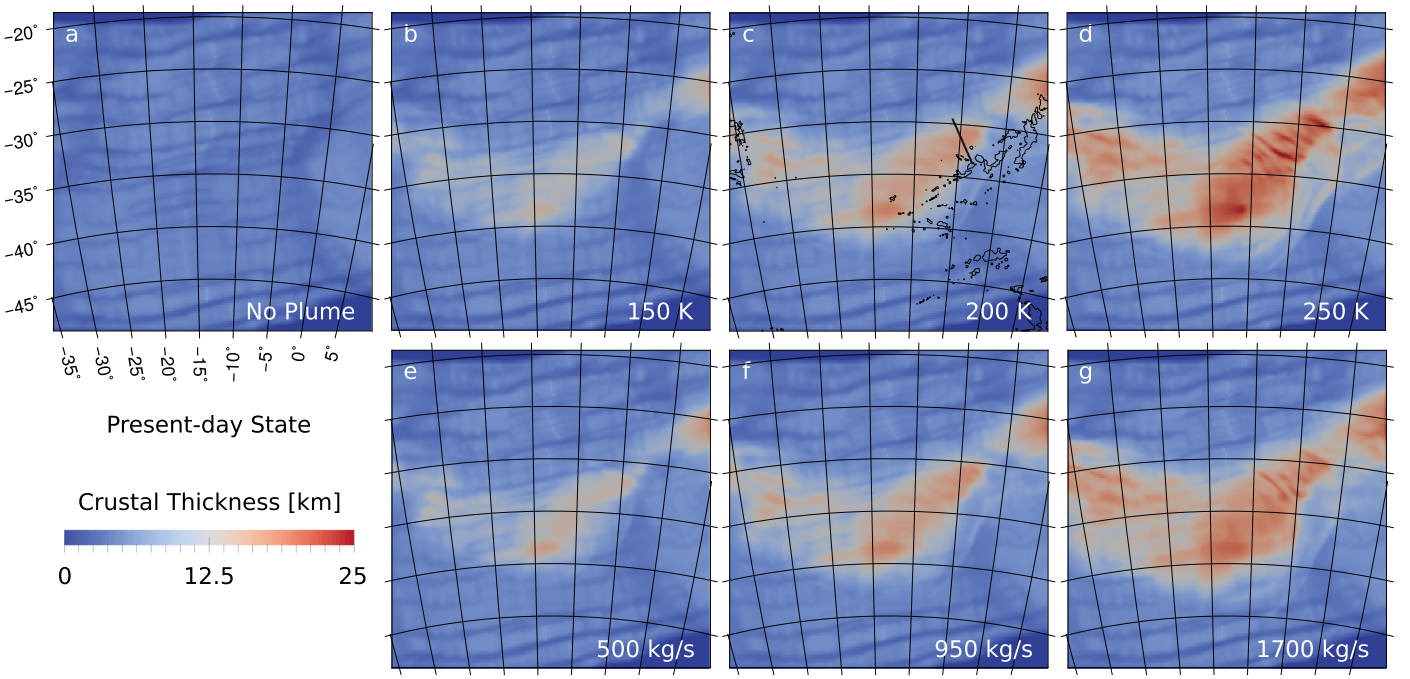

Figure 10. Maps of crustal thickness at present day for models with different plume tail properties and compared to a model without plume influx. The top row displays a model (a) without plume, plume excess temperatures of (b) 150 K, (c) 200 K (the reference case), and (d) 250 K, and the bottoms row shows models with plume buoyancy fluxes of (e) 500 kg/s, (f) 1000 kg/s (the reference case), and (g) 1500 kg/s. The profile through the convection models shown in Figure 11 is marked with a thick black line. The −3300 m contour of topography representing the hotspot track and modified as in Figure 5 are given as thin black lines in Figure 10c. Crustal thickness is computed by passive advection of melt.

of the lithosphere in the model derived from tomographic data depends on the conversion between seismic velocities and temperatures, and therefore might be slightly higher or lower, changing the total melt volume compared to Figure 9b. Also, seismic tomography provides a snapshot at present day and lithosphere thickness may have changed with time. But although the model with a thin lithosphere of only 110 km results in a melt volume that is closest to the observations, we cannot certainly rule out a thicker initial lithosphere because a number of processes that can lead to lithospheric thinning and increase the volume of generated melts are not included in the model. Examples are viscosity reduction due the presence of melt or water, dislocation creep as dominant deformation mechanism, melt migration and freezing, and plasticity, some of which are discussed in previous studies [e.g., *Howell et al.*, 2014; *Nielsen and Hopper*, 2004].

3.5. Constraining Plume Properties by Comparing the Associated Crustal Thickness Variations

Due to the overall agreement of generated crustal thickness and observed topography (section 3.3), it seems plausible to constrain the plume properties by comparing the results of models with different plume excess temperatures and buoyancy fluxes to these observations. As expected, our models show an increase of hotspot activity with both increasing buoyancy flux and excess temperature of the plume (Figure 10). In addition, we find that the temperature seems to have a stronger influence than the inflow volume. While varying the temperature also implies a change in buoyancy flux, a plume with an excess temperature of 150 K and a buoyancy flux of 700 kg/s (Figure 10b) produces less melt than one with an excess temperature of 200 K and a buoyancy flux of 500 kg/s (Figure 10e). The same relation is valid for higher plume excess temperatures. Fitting a linear trend to the integrated crustal thickness in dependence of the buoyancy flux reveals that the temperature change has more than twice the effect than a change of the buoyancy flux alone. For a more complete description of deriving scaling relationships between excess temperature, buoyancy flux and melt flux, we refer to *Ribe and Christensen* [1999].

Comparing profiles of crustal thickness across the hotspot track to seismic profiles (Figure 11) reveals that models with excess temperatures of 200 K or higher and buoyancy fluxes of 1000 kg/s or higher

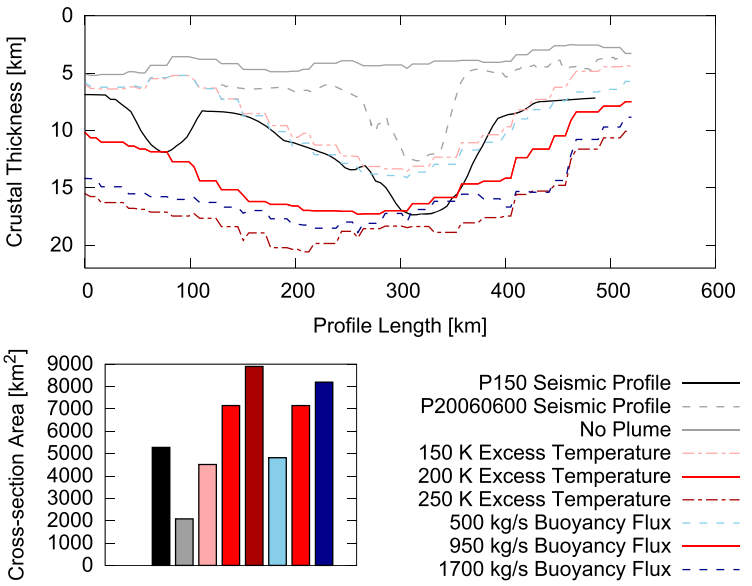

Figure 11. (top) Crustal thickness across the hotspot track for models with different plume tail excess temperatures (lines in different shades of red) and buoyancy fluxes (lines in different shades of blue), compared to a model without plume influx (gray line) and to the crustal thickness derived from seismic models (Profile P150 of *Fromm et al*. [2015] and Profile 20060600 of *Kessling* [2008]). The position of the model profiles is shown in Figure 10c. (bottom) Integrated area of the crustal thickness along the profile. Note that the reference model with 950 kg/s buoyancy flux and 200 K excess temperature appears twice for better comparison. Values in excess of the one in the model without plume (gray bar) reveal the plume influence and how it depends on the plume properties. Crustal thickness is computed by passive advection of melt.

significantly overestimate the produced melt volume. Due to the limited resolution and simplification of melt migration processes, our models are not able to reproduce small-scale features visible in the observations. However, the maximum magmatic crustal thickness of 13–17 km suggested by the seismic profiles indicates that the properties of the Tristan plume tail tend toward the lower end of predicted values for temperature and buoyancy flux. Values of at most 150–200 K respectively 500–700 kg/s achieve reasonable agreement with the profile P150 but are still too high to match profile P20060600. We emphasize that the profile P20060600 by *Kessling* [2008] from 5.5°W, 33.5°S to 2°W, 35.5°S samples a part of the hotspot track that is closer to our model profiles. The profile P150 of *Fromm et al*. [2015] on the other hand (9.2°E, 22.2°S to 5°E, 20.2°S) samples a very thick segment close to the plume-ridge crossing and therefore represents an upper limit on the possible crustal thickness.

3.6. Influence of Global Flow Field

Regional studies of plume-lithosphere interaction usually do not take into account the global mantle flow field [e.g., *Ribe*, 1996; *Ito et al*., 1997; *Albers and Christensen*, 2001; *Ruedas et al*., 2004; *Schmeling and Marquart*, 2008; *Howell et al*., 2014]. Here we investigate this influence on plume-ridge interaction by comparing the reference model to a model without prescribed global flow (as described in section 2.4).

As both model setups are chosen in such a way that the plume-arrival position at the surface agrees with the observed hotspot track (section 2.1), the geometrical pattern of the computed hotspot track is similar in both models. However, there are significant differences in the detailed structure and overall volume of the generated magmatic crust (see Figure 12b). The maximum plume-related crustal thickness is reduced by 30% (across the profile in Figure 12) without the influence of the global flow, and the overall plume-related melt volume in the model region is lower by 40%. This effect can be partly explained by the lower effective buoyancy flux in the model without global flow. However, when correcting for this effect by linear interpolation between the models with different buoyancy fluxes, a contribution of 20% remains that is purely related to the horizontal global flow.

A cross section of the plume (Figure 12a) shows how the global flow can explain the significant deviation in crustal thickness: in the reference model, the westward mantle flow forces the plume material to spread asymmetrically below the lithosphere, supporting westward material transport and hindering eastward transport. This influence increases the tendency of plume material to flow toward the ridge, and therefore to regions with thinner lithosphere. Hence, plume temperatures in the western, shallower part of the plume head are increased by 15–50 K compared to the model without global flow, leading to a higher melt production. Omitting the influence of the global flow field results in a much more symmetrical spreading of plume material. Therefore, more material is pushed eastward into regions of thicker and colder lithosphere, which prevents extensive melting despite the elevated temperatures.

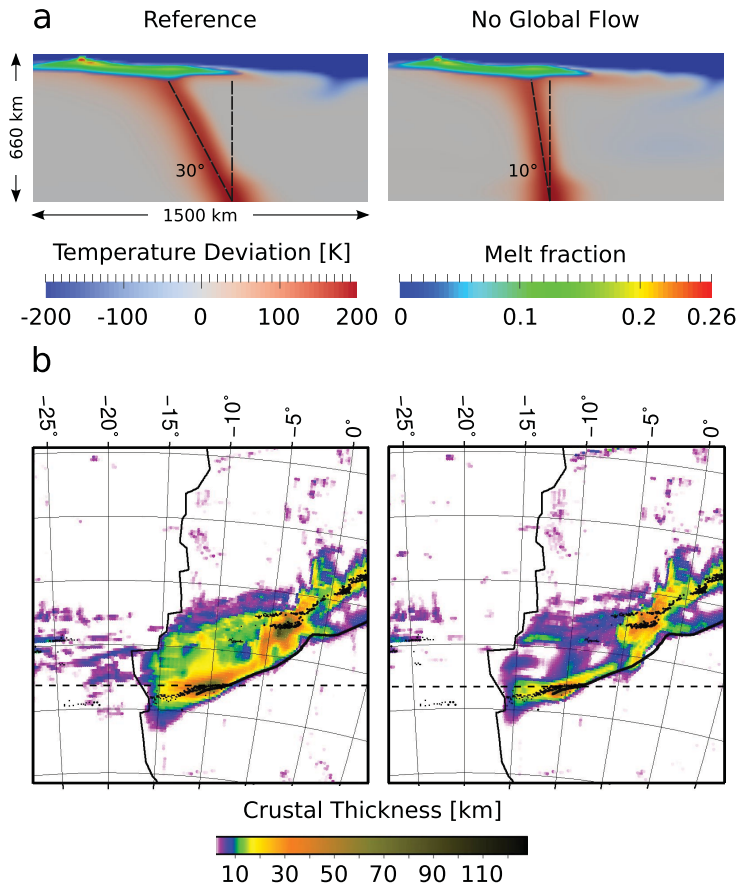

Figure 12. (a) Cross sections through (left) the reference model and (right) a model without global flow, but otherwise unchanged parameters at present day, illustrating the tilt of the plume tail and the melt distribution in the plume head. Temperatures are shown in shades of blue-red and the melt fraction is colored in a different scale, which becomes transparent below melt fractions of 5%. (b) Comparison of crustal thickness maps for the corresponding plume models. The dashed line marks the position of the profile shown in Figure 12a. Crustal thickness is computed by instant melt extraction.

While the position of the transition of the hotspot track into the south-eastward Cape Basin is nearly identical in both models, the thickness of the hotspot track itself is reduced significantly and the transition region into the north-westward Angola Basin is nearly removed in the model without global flow. Instead of producing a wide area or two parallel lines of thickened magmatic crust, mainly the southern line—corresponding to the Gough volcanic chain—is present in the model without global flow, whereas further to the north—corresponding to the Tristan hotspot track—only a rather thin, E-W trending ridge is present. In addition, the models reveal differences in the plume tail position at the base of the upper mantle and in particular in plume shape and tilt: while the present-day plume tail of the reference model is tilted by 30° by the combined effect of plate motion, nearby ridge and global flow (equivalent to a lateral deflection of approximately 300 km), the model without global flow generates a plume tail with a tilt of only 10° (see Figure 12a).

This shows that the influence of global processes on the behavior of regional models is not negligible in regions of strong mantle flow and can lead to differences in predicted melt volumes of up to 40%.

4. Discussion

We explain the distribution of magmatic crust in the South Atlantic by the arrival of a hot mantle plume. Melting in the plume head generates the LIP volcanism, and melting in the plume tail, in interaction with the Mid-Atlantic Ridge, leads to one broad or two smaller lineaments of thickened crust—the hotspot track. When the plume reaches the base of the lithosphere in a sufficient distance from the ridge, two separate regions of upwelling and significant melting are created (see also supporting information Figure S5a): one where the plume tail arrives (the off-ridge track), and another one when the plume material that is sucked toward the ridge reaches the ridge and flows upward (the on-ridge track). This can lead to two parallel lines of volcanic islands, but if one of these melting regions is absent, only one track is generated.

In general, this model fits the observation on a first order. It is able to reproduce and explain the melt distribution and volume in the LIP and hotspot track. However, our plume model generates overall thicker and more prominent hotspot tracks than the maximum width of 100 km of thickened crust observed by *O'Connor and Jokat* [2015a]. On the other hand, the volume of LIP-related melts is relatively low compared to

observations. And although several models feature two parallel lines of increased magmatic activity with similar spacing as the Tristan and Gough tracks, melt is always distributed over a wide area, where observations show the focusing into several distinct, narrower tracks.

4.1. Limitations of the Geodynamic Model

A number of limitations of our modeling approach can explain these differences. While separated melting regions within a distance of a few hundred kilometers are generated in our model, no mechanisms for focusing of melt on a smaller scale of several tens of kilometers are included. Different processes related to porous flow and fracturing have the potential to focus melt into more distinct structures, such as ascent through fractures in the lithosphere, channelized flow due to upwelling melting in a heterogeneous mantle [*Katz and Weatherley*, 2012; *Weatherley and Katz*, 2012] or flexural stresses due to volcanic loading [*Hieronymus and Bercovici*, 2001]. In addition, viscosities in our model plume are higher than in reality to be consistent with the global model that provides the boundary conditions; and resolution is limited to 10 km. This causes larger structures of hot plume material and broader melting regions than expected for a plume of this temperature. Furthermore, these model properties inhibit small-scale convection and viscous fingering instabilities, which can lead to focusing of melt into distinct chains of volcanic activity [e.g., *Ballmer et al*., 2011].

The comparatively low LIP melt volumes in our model can be explained by a number of mechanical and magmatic processes that have the potential to thin the lithosphere and are not included in the present models. Lower viscosities due to a strong temperature dependence, the presence of melt or water, and dislocation creep as an important deformation mechanism all enhance small-scale convection within the hot plume material at the base of the lithosphere [*Moore et al*., 1998, 1999]. Furthermore, the fast transport of magma and the associated latent heat can lead to thermomagmatic erosion of the lithosphere. Freezing melt has a higher density than the surrounding mantle, providing an additional destabilizing effect. Finally, extension during the rifting phase results in faults and thinning of the lithosphere and crust, which is not captured in models without plasticity. All these processes of lithospheric thinning increase the volume of melt produced significantly when hot material rises to regions of shallower depth. Hence, they could easily explain the larger observed magma volumes and igneous crustal thickness for the Paraná-Etendeka LIP compared to our model results.

Two-phase models of magma/mantle dynamics with the capability to simulate plastic and elastic deformation in addition to viscous flow will allow a more detailed investigation of magmatic features of the crust developing in interaction with tectonic processes and the small-scale mechanical structure of the lithosphere as well as more realistic estimates of melt volumes. For example, extracting the generated thick crust could lead to a downward compaction flow that reduces decompression melting [*Schmeling and Marquart*, 2008]. In addition, we neglect any changes in material properties related to retained melt or depletion of the residue. Positive buoyancy of melt and depleted material, low-viscosity channels due to focusing of melt, stiffening of the material due to the extraction of water in the melting process, or changes in chemical composition of the mantle residue from asthenospheric mantle to depleted oceanic lithosphere may further influence the model dynamics. In particular, stiffening of the depleted residue has been suggested to reduce the thickness of crust generated by a plume in interaction with a mid-ocean ridge significantly [*Ito et al*., 1999; *Howell et al*., 2014]. This is a likely explanation for the overly thick modeled crust for times when the plume was located directly below the ridge, while it may not have such an important influence on the volume of LIP-generated melts further away from the ridge.

Another important factor for the amount of melt generated in a geodynamic model is the choice of parametrization for melting in dependence of temperature and pressure, and the assumed composition of the source material. We use the parametrization of *Katz et al*. [2003] for anhydrous peridotite, but other melting models predict different melting rates: *Gregg et al*. [2009] reveal absolute differences in melt fraction of up to 10% between models for a mid-ocean ridge setup. Moreover, both a higher content of water [*Katz et al*., 2003] and recycled crustal material [*Sobolev et al*., 2007, 2011] are known to enhance melt production by several percent. This means that there is a considerable uncertainty in the computed melt volume related to the employed data for mantle melting and the composition of the Tristan plume alone. Nevertheless, the patterns of melt distribution and the general structures of the produced igneous crust should remain largely unaffected.

Moreover, our kinematic surface boundary condition may not appropriately represent rift migration, a possible cause for continental margin asymmetry and crustal hyperextension [*Brune et al*., 2014]. Accordingly, these processes may influence the asymmetry of volcanic rocks generated in the rift between South American and African plates, which may hence not be accurate in our model. Kinematic surface boundary conditions combined with a stress-independent viscosity formulation (as used here) can lead to artificial dissipative heating at the ridge that potentially influences the thermal structure of the lithosphere. We ensured that this effect is small in our models and that the resulting lithospheric temperature profile is consistent with published estimates [e.g., *McKenzie et al*., 2005].

Our models provide an explanation for the crustal thickness jump that is observed across the FFZ: ascending plume material flowing into the opening rift leads to higher melt generation south of the fracture zone. However, it is important to note that the seismic profile is located within the continent ocean transition (COT) south of the ridge (in the Cape Basin) and at normal oceanic crust north of it in the Angola Basin. The nature of the thick COT crust is still debated. Hence, part of the north-south variation of crustal thickness might be due to the presence of a significant portion of continental crust in the profile south of the ridge. This could be one reason for the smaller crustal thickness jump in our models when compared to seismic profiles.

4.2. Limitations of the Hotspot Motion Model

Other detailed features, such as the timing of the ridge jump and the associated separation of the hotspot track to the two continents, and the precise position of the generated crust are linked to the accuracy of the employed hotspot motion model. However, we only used the position of the Paraná-Etendeka LIP and large-scale mantle flow based on tomographic models to reconstruct the plume position. This allows for different scenarios, each explaining certain features of the hotspot track (Figure 7).

For example, before the ridge crossing the hotspot presumably was closer to the ridge than it is simulated in our reference model. Thus, the model does not reproduce the beginning of the observed Walvis Ridge on the African side, and the prominent area of very thick magmatic crust related to this crossing is generated approximately 2° further to the west and south, respectively. Related to that, on the South American side, the Rio Grande Rise is clearly separated from the continent in the observations, whereas our results predict a more continuous track from the continent, because in our model the plume was initially beneath the South American plate.

Nevertheless, some features are fit better by some of our models than others (Figure 7): model Track2 explains the older part of the Walvis Ridge on the African plate—a single ridge reaching all the way to the continent, including the position of the strongly thickened crust related to the plume-ridge crossing—better, because in this hotspot motion model the plume has remained close to the ridge before 90 Ma. In contrast, the reference plume location further west in combination with westward large-scale flow leads to much less volcanism and no continuous track on the African plate before 90 Ma. Model RefShift explains the location of the younger part of the track much better. This may indicate a plume location closer to Gough Island, whereas the generation of Tristan da Cunha would be due to plume-ridge interaction. Consequently, none of our models fits all of the observed volcanism, but different models fit different parts. Fitting the position of the inflowing plume material to the hotspot track (possibly closer to Gough Island) would presumably lead to even better agreement of small-scale structures.

However, reconstructing the plume position is not straightforward. One effect that needs to be considered—for example when devising hotspot reference frames—is that volcanism may occur several million years after lithosphere has passed over the plume. For example, in Figure 6, bottom, the hotspot track age for the lithosphere generated around 5°E 27°S during plume-ridge crossing at ≈90 Ma is only 70–80 Ma, because melts continued to be generated beneath that lithosphere. These younger model ages help to explain the discrepancy between measured ages near that location and the hotspot track of *Doubrovine et al*. [2012].

Moreover, we have shown that a single plume can cause several volcanic chains, and that the observed magmatic activity does not always have to be directly above the plume conduit. If the plume tail reaches the base of the lithosphere close to the mid-ocean ridge, and global mantle flow supports flow toward the ridge, plumes may temporarily only generate an on-ridge track, whereas the off-ridge track directly above

the hotspot can be entirely absent during that time. This means that discrepancies between hotspot motion models and observed volcanism may hence not be due to a deficiency of the model reference frame but due to plume-ridge interaction. One example in our model could be the track on the African side, directly after the plume crossed (and while it is still close to) the ridge: The predicted track of *Doubrovine et al*. [2012] is southeast of the observed track in that area, but the distribution of generated melt in our model agrees well with the observations. This shows the importance of our results for hotspot motion models and hotspot reference frames, which are usually constructed under the assumption that the plume is directly beneath the track.

4.3. Alternative Models

Our model explains the generation of separate volcanic chains close to mid-ocean ridges by disconnected melting regions below the lithosphere while the plume material is spreading preferentially toward the ridge. Other mechanisms have been proposed to explain the observed splitting of hotspot tracks in other regions. Small-scale convection could lead to a separation of melt upwelling with a characteristic length scale. However, small-scale convection usually only occurs below plates older than 70 Ma [*Ballmer et al*., 2011], while the oceanic plate above the Tristan plume is much younger. Nevertheless, the reduced viscosity in the plume head enhances small-scale convection and can lead to a shear-aligned roll regime of material flow with a spacing of a few hundred kilometers [*Moore et al*., 1998]. For the Tristan plume, which has a low excess temperature of $<$180 K and impinges on a young plate with an age of approximately 20 Ma, convection rolls are not expected to occur closer than 500 km downstream of the plume center [*Moore et al*., 1998; *Agrusta et al*., 2013]. This would require the plume tail to be at least 500 km upstream of the centers of volcanic activity. For the current position of Tristan, upstream with respect to the local flow field would mean a distance of at least 1000 km from the mid-ocean ridge, which would presumably be too large for the plume material to still flow toward the ridge. Upstream with respect to the plate motion would mean a plume position directly below the ridge, which would be visible in numerous observations. Alternatively, several smaller, separated plumes have been suggested by *O'Connor et al*. [2012]. Yet a consistent dynamic model, a potential mechanism, or an estimate for the forces required to prevent such small plumes from merging during their ascent are still missing. For other volcanic chains, volcanic loading and lithospheric flexure have been suggested as mechanisms for splitting the volcanism caused by a single plume into a dual line [*Hieronymus and Bercovici*, 1999]. However, this causes volcanic lines with a much closer spacing ($\approx$70 km) than the Tristan-Gough chains ($\approx$500 km). Another mechanism for the formation of seamount chains and the material transport from an off-ridge plume to the mid-ocean ridge are viscous fingering instabilities—formed when low-viscous plume material is injected into the asthenosphere [*Weeraratne et al*., 2007]—and the associated shear-driven upwelling [*Ballmer et al*., 2013]. But while these instabilities might generate volcanic chains with the observed spacing, they are expected to lead to much faster age progression than observed for the Tristan and Gough tracks. Moreover, over the last 90 Ma, the closest ridge segment from the plume tail, and therefore the expected direction of fingering instabilities, was located in north-westward direction—perpendicular to the direction of the Tristan-Gough lineaments and the absolute plate motion. Last, an additional depleted/dehydrated mantle region can form below an active hotspot due to the continuous melting and lead to a shift of the melting region to both sides of this "plug" [*Kundargi and Hall*, 2014], but the continuous plate movement should transport this "plug" away and lead to an oscillating behavior of the hotspot tracks.

Therefore, we think that our mechanism is a likely explanation for the separation of the Tristan and Gough volcanic chains. In addition, it does not contradict the observation of a distinct geochemical signature for each of the two tracks [*Hoernle et al*., 2015], because a single plume can carry two distinct chemical components from the CMB to the surface without significant mixing [*Farnetani and Hofmann*, 2010]. But even though we rule out the discussed alternative models as the main mechanism for separating the Tristan plume into the Tristan and Gough track, they might still have an influence on focusing melt into more distinct structures.

Although we specifically study the Tristan hotspot and its interaction with the South Atlantic opening, some of our results—in particular the strong influence of large-scale mantle flow on plume-ridge interaction—can be readily generalized. Our method can be easily adopted to study plume-ridge interaction for other hotspots close to mid-ocean ridges, like Galápagos, Réunion, Kerguelen, or Iceland. All of these hotspots are very promising candidates for further studies due to their complex histories of interactions with close-by

ridges. These investigations could help to understand the behavior of plumes below fast-moving plates, forces exchanged between plumes and plates, the role of plumes in subduction initiation, the generation of new plate boundaries on top of mantle plumes, and the history of plumes over longer periods of time.

5. Conclusion

We have studied the evolution of the Tristan plume and its interaction with the Mid-Atlantic Ridge in a series of three-dimensional regional convection models, and in particular the influence of the global flow field on the distribution of magmatism. Our comparison of computed crustal thickness to maps of residual topography and seismic profiles has shown that a convection model that takes into account plate motion, mantle flow, plume movement, and decompression melting of peridotite resembles both the current-day geometry of the hotspot track and the distribution of syn-rift magmatism. This includes the correct timing of the ridge overriding the plume, the east-west distribution of melts of the Paraná-Etendeka flood basalts, with a majority of the plume-related melt being generated on the South American plate, and differences in crustal thickness across the Florianopolis Fracture Zone. Moreover, the comparison to seismic profiles allowed us to further constrain the physical properties of the Tristan mantle plume within the existing uncertainties.

Our key findings are as follows:

1. The broadening of the Tristan hotspot track and the apparent separation into the Tristan and Gough volcanic chains can be explained by the interaction of a single plume with the nearby ridge. The global flow field enhances material motion from below the off-ridge track toward the ridge and regions of thinner lithosphere, where decompression melting leads to the development of a broad region of volcanic activity, which can be focused into additional volcanic chains.
2. The jump in crustal thickness north and south of the Florianopolis Fracture Zone is well reproduced by hot plume material in the asthenosphere feeding into the already opening southern part of the rift. 10–15 Ma later—when the northern part opens—the plume head has cooled and has been transported away from the rift, leading to a lower crustal production north of the FFZ.
3. An excess temperature of 150 K and a buoyancy flux of around 500 kg/s—consistent with the lower end of previously published estimates for the Tristan hotspot—lead to a crustal production comparable to seismic observations for the Tristan hotspot track. Larger plumes overpredict the generated crustal thickness in our models.
4. A back-rotated lithosphere model explains the size and extent of the Etendeka LIP better than a constant lithosphere thickness. However, in this model, the thick lithosphere north of the PEFZ prevents the Paraná LIP from extending westward and northward, as it is observed for the LIP today. Additional high-resolution studies are needed to investigate if a more advanced simulation of the fault zone with a stronger and more localized thinning of the lithosphere would produce a better agreement between model and observation.
5. The position and shape of the generated large igneous province is an additional constraint for the plate reference frame used: our reference model approximately fits the Paraná LIP location; with the same reference frame and strong initial lithosphere thickness variations, volcanism occurs near the Etendeka LIP.
6. Neglecting global mantle flow can influence the estimates of plume temperature by up to 50 K and mispredict the plume tilt by up to 20°. This can prevent the development of two separate volcanic chains in the geodynamic model. Additionally incorporating global flow changes (in this case increases), the overall volume of plume-related melt by 40%, with 20% being purely caused by the westward lateral flow.

The current models are simplified and neglect plastic behavior of the lithosphere and melt segregation, which limits focusing of melt and prevents thinning of the lithosphere by thermomagmatic erosion. Despite these limitations, the results presented here indicate that regional convection models incorporating plate motion and global mantle flow can resemble the melt distribution both of the large igneous province and the hotspot track, including small-scale features such as the development of several distinct volcanic chains. Hence, this method promises to be a useful tool to investigate unresolved questions surrounding other hotspots with a complex history of origins.

Acknowledgments
The geodynamic models were computed with the open-source software ASPECT (http://aspect.dealii.org) and visualized with the open-source programs ParaView (http://www.paraview.org) and GMT [*Wessel et al*., 2013]. The necessary data to reproduce the models is included in the supporting information. We are grateful to Tanja Fromm, Wolfgang Bangerth, and Thorsten Becker for carefully and critically reading the manuscript and providing suggestions for improvement. We would also like to thank Maxim Ballmer, Harro Schmeling, Mike Gurnis and an anonymous reviewer for their helpful comments. This project was funded by the Deutsche Forschungsgemeinschaft (DFG) under grant STE 907/8-2 as part of the DFG Priority Program SPP 1375 "South Atlantic Margin Processes and Links with onshore Evolution" and grant STE 907/11-1 to B.S. The computational resources were provided by the North-German Supercomputing Alliance (HLRN) as part of the project "Plume-Plate interaction in 3D mantle flow—Revealing the role of internal plume dynamics on global hot spot volcanism." T.H.T. and B.S. also acknowledge the European Research Council under the European Union's Seventh Framework Programme (FP7/2007-2013)/European Research Council Advanced Grant Agreement 267631 (Beyond Plate Tectonics) and the Research Council of Norway through its Centres of Excellence funding scheme (Centre for Earth Evolution and Dynamics, 223272) for financial support. J.D. acknowledges the support of the Computational Infrastructure in Geodynamics (CIG-II) grant (National Science Foundation Award EAR-0949446, via The University of California – Davis) and the Helmholtz graduate research school GeoSim.

References

Agrusta, R., D. Arcay, A. Tommasi, A. Davaille, N. Ribe, and T. Gerya (2013), Small-scale convection in a plume-fed low-viscosity layer beneath a moving plate, *Geophys. J. Int.*, *194*, 591–610, doi:10.1093/gji/ggt128.

Albers, M., and U. R. Christensen (2001), Channeling of plume flow beneath mid-ocean ridges, *Earth Planet. Sci. Lett.*, *187*, 207–220, doi:10.1016/S0012-821X(01)00276-X.

Assumpção, M., M. Feng, A. Tassara, and J. Julià (2013), Models of crustal thickness for South America from seismic refraction, receiver functions and surface wave tomography, *Tectonophysics*, *609*, 82–96, doi:10.1016/j.tecto.2012.11.014.

Ballmer, M. D., G. Ito, J. van Hunen, and P. J. Tackley (2011), Spatial and temporal variability in Hawaiian hotspot volcanism induced by small-scale convection, *Nat. Geosci.*, *4*, 457–460, doi:10.1038/ngeo1187.

Ballmer, M. D., C. P. Conrad, E. I. Smith, and N. Harmon (2013), Non-hotspot volcano chains produced by migration of shear-driven upwelling toward the East Pacific Rise, *Geology*, *41*(4), 479–482, doi:10.1130/G33804.1.

Bangerth, W., T. Heister, et al. (2015), *ASPECT: Advanced Solver for Problems in Earth's ConvecTion*, Comput. Infrastructure for Geodyn.

Becker, K., D. Franke, R. Trumbull, M. Schnabel, I. Heyde, B. Schreckenberger, H. Koopmann, K. Bauer, W. Jokat, and C. M. Krawczyk (2014), Asymmetry of high-velocity lower crust on the South Atlantic rifted margins and implications for the interplay of magmatism and tectonics in continental breakup, *Solid Earth*, *5*, 1011–1026, doi:10.5194/se-5-1011-2014.

Becker, T. W., and L. Boschi (2002), A comparison of tomographic and geodynamic mantle models, *Geochem. Geophys. Geosyst.*, *3*(1), 1003, doi:10.1029/2001GC000168.

Braitenberg, C. (2015), Exploration of tectonic structures with GOCE in Africa and across-continents, *Int. J. Appl. Earth Obs. Geoinf.*, *35*, 88–95, doi:10.1016/j.jag.2014.01.013.

Brune, S., C. Heine, M. Pérez-Gussinyé, and S. V. Sobolev (2014), Rift migration explains continental margin asymmetry and crustal hyperextension, *Nat. Commun.*, *5*, 4014, doi:10.1038/ncomms5014.

Bryan, S. E., and R. E. Ernst (2008), Revised definition of Large Igneous Provinces (LIPs), *Earth Sci. Rev.*, *86*, 175–202, doi:10.1016/j.earscirev.2007.08.008.

Buiter, S. (2014), Geodynamics: How plumes help to break plates, *Nature*, *513*, 36–37, doi:10.1038/513036a.

Burov, E., and T. Gerya (2014), Asymmetric three-dimensional topography over mantle plumes, *Nature*, *513*, 85–89, doi:10.1038/nature13703.

Chulick, G. S., S. Detweiler, and W. D. Mooney (2013), Seismic structure of the crust and uppermost mantle of South America and surrounding oceanic basins, *J. South Am. Earth Sci.*, *42*, 260–276, doi:10.1016/j.jsames.2012.06.002.

Coffin, M. F., R. A. Duncan, O. Eldholm, J. G. Fitton, F. A. Frey, H. C. Larsen, J. J. Mahoney, A. D. Saunders, R. Schlich, and P. J. Wallace (2006), Large igneous provinces and scientific ocean drilling: Status quo and a look ahead, *Oceanography*, *19*(4), 150–160, doi:10.5670/oceanog.2006.13.

Connolly, J. A. D. (2005), Computation of phase equilibria by linear programming: A tool for geodynamic modeling and its application to subduction zone decarbonation, *Earth Planet. Sci. Lett.*, *236*, 524–541, doi:10.1016/j.epsl.2005.04.033.

Courtillot, V., C. Jaupart, I. Manighetti, P. Tapponnier, and J. Besse (1999), On causal links between flood basalts and continental breakup, *Earth Planet. Sci. Lett.*, *166*, 177–195, doi:10.1016/S0012-821X(98)00282-9.

Davies, G. F. (1988), Ocean bathymetry and mantle convection: 1. Large-scale flow and hotspots, *J. Geophys. Res.*, *93*(B9), 10,467–10,480, doi:10.1029/JB093iB09p10467.

de Assis Janasi, V., V. A. de Freitas, and L. H. Heaman (2011), The onset of flood basalt volcanism, Northern Paraná Basin, Brazil: A precise U-Pb baddeleyite/zircon age for a Chapecó-type dacite, *Earth Planet. Sci. Lett.*, *302*, 147–153, doi:10.1016/j.epsl.2010.12.005.

Doubrovine, P. V., B. Steinberger, and T. H. Torsvik (2012), Absolute plate motions in a reference frame defined by moving hot spots in the Pacific, Atlantic, and Indian oceans, *J. Geophys. Res.*, *117*, B09101, doi:10.1029/2011JB009072.

Farnetani, C. G., and A. W. Hofmann (2010), Dynamics and internal structure of the Hawaiian plume, *Earth Planet. Sci. Lett.*, *295*, 231–240, doi:10.1016/j.epsl.2010.04.005.

Fromm, T., L. Planert, W. Jokat, T. Ryberg, J. H. Behrmann, M. H. Weber, and C. Haberland (2015), South Atlantic opening: A plume-induced breakup?, *Geology*, *43*(10), 931–934, doi:10.1130/G36936.1.

Gibson, S. A., R. N. Thompson, and J. A. Day (2006), Timescales and mechanisms of plume–lithosphere interactions: $^{40}Ar/^{39}Ar$ geochronology and geochemistry of alkaline igneous rocks from the Paraná–Etendeka large igneous province, *Earth Planet. Sci. Lett.*, *251*, 1–17, doi:10.1016/j.epsl.2006.08.004.

Gladczenko, T. P., K. Hinz, O. Eldholm, H. Meyer, S. Neben, and J. Skogseid (1997), South Atlantic volcanic margins, *J. Geol. Soc.*, *154*, 465–470, doi:10.1144/gsjgs.154.3.0465.

Gregg, P. M., M. D. Behn, J. Lin, and T. L. Grove (2009), Melt generation, crystallization, and extraction beneath segmented oceanic transform faults, *J. Geophys. Res.*, *114*, B11102, doi:10.1029/2008JB006100.

Heit, B., X. Yuan, M. Weber, W. Geissler, W. Jokat, B. Lushetile, and K.-H. Hoffmann (2015), Crustal thickness and Vp/Vs ratio in NW Namibia from receiver functions: Evidence for magmatic underplating due to mantle plume-crust interaction, *Geophys. Res. Lett.*, *42*, 3330–3337, doi:10.1002/2015GL063704.

Herzberg, C., and P. D. Asimow (2008), Petrology of some oceanic island basalts: PRIMELT2.XLS software for primary magma calculation, *Geochem. Geophys. Geosyst.*, *9*, Q09001, doi:10.1029/2008GC002057.

Herzberg, C., and E. Gazel (2009), Petrological evidence for secular cooling in mantle plumes, *Nature*, *458*, 619–622, doi:10.1038/nature07857.

Hieronymus, C. F., and D. Bercovici (1999), Discrete alternating hotspot islands formed by interaction of magma transport and lithospheric flexure, *Nature*, *397*, 604–607, doi:10.1038/17584.

Hieronymus, C. F., and D. Bercovici (2001), A theoretical model of hotspot volcanism: Control on volcanic spacing and patterns via magma dynamics and lithospheric stresses, *J. Geophys. Res.*, *106*(B1), 683–702, doi:10.1029/2000JB900355.

Hoernle, K., J. Rohde, F. Hauff, D. Garbe-Schönberg, S. Homrighausen, R. Werner, and J. P. Morgan (2015), How and when plume zonation appeared during the 132 Myr evolution of the Tristan hotspot, *Nat. Commun.*, *6*, 7799, doi:10.1038/ncomms8799.

Howell, S. M., G. Ito, A. J. Breivik, A. Rai, R. Mjelde, B. Hanan, K. Sayit, and P. Vogt (2014), The origin of the asymmetry in the Iceland hotspot along the Mid-Atlantic Ridge from continental breakup to present-day, *Earth Planet. Sci. Lett.*, *392*, 143–153, doi:10.1016/j.epsl.2014.02.020.

Ito, G., J. Lin, and C. W. Gable (1997), Interaction of mantle plumes and migrating mid-ocean ridges: Implications for the Galápagos plume-ridge system, *J. Geophys. Res.*, *102*(B7), 15,403–15,417, doi:10.1029/97JB01049.

Ito, G., Y. Shen, G. Hirth, and C. J. Wolfe (1999), Mantle flow, melting, and dehydration of the Iceland mantle plume, *Earth Planet. Sci. Lett.*, *165*(1), 81–96, doi:10.1016/S0012-821X(98)00216-7.

Katz, R. F., and S. M. Weatherley (2012), Consequences of mantle heterogeneity for melt extraction at mid-ocean ridges, *Earth Planet. Sci. Lett.*, *335–336*, 226–237, doi:10.1016/j.epsl.2012.04.042.
Katz, R. F., M. Spiegelman, and C. H. Langmuir (2003), A new parameterization of hydrous mantle melting, *Geochem. Geophys. Geosyst.*, *4*(9), 1073, doi:10.1029/2002GC000433.
Kessling, S. (2008), Die Tiefenstruktur der Kruste des Discovery Seamounts und des südlichen Walfischrückens im Südatlantik, Master's thesis, Friedrich-Schiller-Univ., Jena, Germany.
Kronbichler, M., T. Heister, and W. Bangerth (2012), High accuracy mantle convection simulation through modern numerical methods, *Geophys. J. Int.*, *191*(1), 12–29, doi:10.1111/j.1365-246X.2012.05609.x.
Kundargi, R., and P. S. Hall (2014), Geographic patterns of volcanism at intraplate hotspots, Abstract DI34A-04 presented at 2014 Fall Meeting, AGU, San Francisco.
Lin, S.-C., and P. E. van Keken (2006), Dynamics of thermochemical plumes: 1. Plume formation and entrainment of a dense layer, *Geochem. Geophys. Geosyst.*, *7*, Q02006, doi:10.1029/2005GC001071.
McKenzie, D., J. Jackson, and K. Priestley (2005), Thermal structure of oceanic and continental lithosphere, *Earth Planet. Sci. Lett.*, *233*(3–4), 337–349, doi:10.1016/j.epsl.2005.02.005.
Mihalffy, P., B. Steinberger, and H. Schmeling (2008), The effect of the large-scale mantle flow field on the Iceland hotspot track, *Tectonophysics*, *447*, 5–18, doi:10.1016/j.tecto.2006.12.012.
Moore, W. B., G. Schubert, and P. Tackley (1998), Three-dimensional simulations of plume-lithosphere interaction at the Hawaiian swell, *Science*, *279*, 1008–1011, doi:10.1126/science.279.5353.1008.
Moore, W. B., G. Schubert, and P. J. Tackley (1999), The role of rheology in lithospheric thinning by mantle plumes, *Geophys. Res. Lett.*, *26*(8), 1073–1076, doi:10.1029/1999GL900137.
Morgan, J. P., J. Hasenclever, and C. Shi (2013), New observational and experimental evidence for a plume-fed asthenosphere boundary layer in mantle convection, *Earth Planet. Sci. Lett.*, *366*, 99–111, doi:10.1016/j.epsl.2013.02.001.
Morgan, W. J. (1971), Convection plumes in the lower mantle, *Nature*, *230*, 42–43, doi:10.1038/230042a0.
Morgan, W. J. (1978), Rodriguez, Darwin, Amsterdam,. . ., A second type of Hotspot Island, *J. Geophys. Res.*, *83*(B11), 5355–5360, doi:10.1029/JB083iB11p05355.
Müller, R. D., M. Sdrolias, C. Gaina, and W. R. Roest (2008), Age, spreading rates, and spreading asymmetry of the world's ocean crust, *Geochem. Geophys. Geosyst.*, *9*, Q04006, doi:10.1029/2007GC001743.
Nielsen, T. K., and J. R. Hopper (2004), From rift to drift: Mantle melting during continental breakup, *Geochem. Geophys. Geosyst.*, *5*, Q07003, doi:10.1029/2003GC000662.
O'Connor, J. M., and R. A. Duncan (1990), Evolution of the Walvis Ridge-Rio Grande Rise Hot Spot System: Implications for African and South American plate motions over plumes, *J. Geophys. Res.*, *95*(B11), 17,475–17,502, doi:10.1029/JB095iB11p17475.
O'Connor, J. M., and W. Jokat (2015a), Tracking the Tristan-Gough mantle plume using discrete chains of intraplate volcanic centers buried in the Walvis Ridge, *Geology*, *43*(8), 715–718, doi:10.1130/G36767.1.
O'Connor, J. M., and W. Jokat (2015b), Age distribution of Ocean Drill sites across the Central Walvis Ridge indicates plate boundary control of plume volcanism in the South Atlantic, *Earth Planet. Sci. Lett.*, *424*, 179–190, doi:10.1016/j.epsl.2015.05.021.
O'Connor, J. M., and A. P. le Roex (1992), South Atlantic hot spot-plume systems: 1. Distribution of volcanism in time and space, *Earth Planet. Sci. Lett.*, *113*, 343–364, doi:10.1016/0012-821X(92)90138-L.
O'Connor, J. M., W. Jokat, A. P. le Roex, C. Class, J. R. Wijbrans, S. Keßling, K. F. Kuiper, and O. Nebel (2012), Hotspot trails in the South Atlantic controlled by plume and plate tectonic processes, *Nat. Geosci.*, *5*, 735–738, doi:10.1038/ngeo1583.
Peate, D. W. (1997), The Paraná-Etendeka Province, in *Large Igneous Provinces: Continental, Oceanic, and Planetary Flood Volcanism*, edited by J. J. Mahoney and M. F. Coffin, pp. 217–245, AGU, Washington, D. C., doi:10.1029/GM100p0217.
Putirka, K. (2008), Excess temperatures at ocean islands: Implications for mantle layering and convection, *Geology*, *36*(4), 283–286, doi:10.1130/G24615A.1.
Ribe, N. M. (1996), The dynamics of plume-ridge interaction: 2. Off-ridge plumes, *J. Geophys. Res.*, *101*(B7), 16,195–16,204, doi:10.1029/96JB01187.
Ribe, N. M., and U. R. Christensen (1999), The dynamical origin of Hawaiian volcanism, *Earth Planet. Sci. Lett.*, *171*(4), 517–531, doi:10.1016/S0012-821X(99)00179-X.
Richards, M. A., R. A. Duncan, and V. E. Courtillot (1989), Flood basalts and hot-spot tracks: Plume heads and tails, *Science*, *246*, 103–107, doi:10.1126/science.246.4926.103.
Ringwood, A. E., and T. Irifune (1988), Nature of the 650-km seismic discontinuity: implications for mantle dynamics and differentiation, *Nature*, *331*, 131–136, doi:10.1038/331131a0.
Rohde, J. K., P. van den Bogaard, K. Hoernle, F. Hauff, and R. Werner (2013), Evidence for an age progression along the Tristan-Gough volcanic track from new $^{40}Ar/^{39}Ar$ ages on phenocryst phases, *Tectonophysics*, *604*, 60–71, doi:10.1016/j.tecto.2012.08.026.
Ruedas, T., H. Schmeling, G. Marquart, A. Kreutzmann, and A. Junge (2004), Temperature and melting of a ridge-centred plume with application to Iceland. Part I: Dynamics and crust production, *Geophys. J. Int.*, *158*(2), 729–743, doi:10.1111/j.1365-246X.2004.02311.x.
Ryberg, T., C. Haberland, T. Haberlau, M. H. Weber, K. Bauer, J. H. Behrmann, and W. Jokat (2015), Crustal structure of northwest Namibia: Evidence for plume-rift-continent interaction, *Geology*, *43*(8), 739–742, doi:10.1130/G36768.1.
Schilling, J.-G. (1991), Fluxes and excess temperatures of mantle plumes inferred from their interaction with migrating mid-ocean ridges, *Nature*, *352*, 397–403, doi:10.1038/352397a0.
Schmeling, H., and G. Marquart (2008), Crustal accretion and dynamic feedback on mantle melting of a ridge centred plume: The Iceland case, *Tectonophysics*, *447*, 31–52, doi:10.1016/j.tecto.2006.08.012.
Sleep, N. H. (1990), Hotspots and mantle plumes: Some phenomenology, *J. Geophys. Res.*, *95*(B5), 6715–6736, doi:10.1029/JB095iB05p06715.
Sleep, N. H. (1997), Lateral flow and ponding of starting plume material, *J. Geophys. Res.*, *102*(B5), 10,001–10,012, doi:10.1029/97JB00551.
Sleep, N. H. (2002), Ridge-crossing mantle plumes and gaps in tracks, *Geochem. Geophys. Geosyst.*, *3*(12), 8505, doi:10.1029/2001GC000290.
Sobolev, A. V., et al. (2007), The amount of recycled crust in sources of mantle-derived melts, *Science*, *316*, 412–417, doi:10.1126/science.1138113.
Sobolev, S. V., A. V. Sobolev, D. V. Kuzmin, N. A. Krivolutskaya, A. G. Petrunin, N. T. Arndt, V. A. Radko, and Y. R. Vasiliev (2011), Linking mantle plumes, large igneous provinces and environmental catastrophes, *Nature*, *477*, 312–316, doi:10.1038/nature10385.
Steinberger, B., and A. R. Calderwood (2006), Models of large-scale viscous flow in the Earth's mantle with constraints from mineral physics and surface observations, *Geophys. J. Int.*, *167*(3), 1461–1481, doi:10.1111/j.1365-246X.2006.03131.x.
Steinberger, B., R. Sutherland, and R. J. O'Connell (2004), Prediction of Emperor-Hawaii seamount locations from a revised model of global plate motion and mantle flow, *Nature*, *430*(6996), 167–173, doi:10.1038/nature02660.

Stixrude, L., and C. Lithgow-Bertelloni (2011), Thermodynamics of mantle minerals—II. Phase equilibria, *Geophys. J. Int.*, *184*(3), 1180–1213, doi:10.1111/j.1365-246X.2010.04890.x.

Tan, E., E. Choi, P. Thoutireddy, M. Gurnis, and M. Aivazis (2006), GeoFramework: Coupling multiple models of mantle convection within a computational framework, *Geochem. Geophys. Geosyst.*, *7*, Q06001, doi:10.1029/2005GC001155.

Thiede, D. S., and P. M. Vasconcelos (2010), Paraná flood basalts: Rapid extrusion hypothesis confirmed by new $^{40}Ar/^{39}Ar$ results, *Geology*, *38*(8), 747–750, doi:10.1130/G30919.1.

Torsvik, T. H., and L. R. M. Cocks (2013), Gondwana from top to base in space and time, *Gondwana Res.*, *24*, 999–1030, doi:10.1016/j.gr.2013.06.012.

Torsvik, T. H., M. A. Smethurst, K. Burke, and B. Steinberger (2006), Large igneous provinces generated from the margins of the large low-velocity provinces in the deep mantle, *Geophys. J. Int.*, *167*(3), 1447–1460, doi:10.1111/j.1365-246X.2006.03158.x.

Torsvik, T. H., S. Rousse, C. Labails, and M. A. Smethurst (2009), A new scheme for the opening of the South Atlantic Ocean and the dissection of an Aptian salt basin, *Geophys. J. Int.*, *177*, 1315–1333, doi:10.1111/j.1365-246X.2009.04137.x.

Torsvik, T. H., B. Steinberger, M. Gurnis, and C. Gaina (2010), Plate tectonics and net lithosphere rotation over the past 150 My, *Earth Planet. Sci. Lett.*, *291*, 106–112, doi:10.1016/j.epsl.2009.12.055.

Weatherley, S. M., and R. F. Katz (2012), Melting and channelized magmatic flow in chemically heterogeneous, upwelling mantle, *Geochem. Geophys. Geosyst.*, *13*, Q0AC18, doi:10.1029/2011GC003989.

Weeraratne, D. S., D. W. Forsyth, Y. Yang, and S. C. Webb (2007), Rayleigh wave tomography beneath intraplate volcanic ridges in the south pacific, *J. Geophys. Res.*, *112*, B06303, doi:10.1029/2006JB004403.

Wegener, A. (1915), *Die Entstehung der Kontinente und Ozeane*, 1st ed., Friedrich Vieweg & Sohn, Braunschweig, Germany.

Wessel, P., W. H. F. Smith, R. Scharroo, J. Luis, and F. Wobbe (2013), Generic mapping tools: Improved version released, *Eos Trans. AGU*, *94*(45), 409–410, doi:10.1002/2013EO450001.